Observations of Wave Energy Dissipation by Bottom Friction on Rocky Shores

Olavo B. Marques,[a, b] Falk Feddersen,[a] James MacMahan,[b] César A. Acevedo-Ramirez,[c] Sutara H. Suanda,[c]

[a] *Scripps Institution of Oceanography, University of California, San Diego, La Jolla, California, USA*

[b] *Oceanography Department, Naval Postgraduate School, Monterey, California, USA*

[c] *Department of Physics and Physical Oceanography, University of North Carolina Wilmington, Wilmington, North Carolina, USA*

Corresponding author: Olavo B. Marques, omarques@ucsd.edu

ABSTRACT: Nearshore wave dissipation by bottom friction can significantly attenuate surface waves when seabed roughness is large. Wave dissipation is parameterized with a friction factor f_e, depending upon the wave orbital excursion at the seabed A_b, and the seabed roughness k_N. Parameterizations have been developed assuming small roughness k_N relative to A_b, but whether they yield accurate f_e for rough seabeds, such as rocky shores, is unclear. Observations from a month-long experiment measured wave transformation on a rough rocky shore, with a large standard deviation of bottom depth σ_h of 0.5–1.5 m. The explicit f_e dependence on variable rocky seabed σ_h has yet to be demonstrated. Sea-swell energy flux consistently decays shoreward of 8 m water depth, which is well offshore of the surfzone given the time-mean incident significant wave height of 1 m. The observed cross-shore flux convergence yields f_e estimates across the instrument array. Quality control criteria are implemented to reduce noise in estimated f_e. Hourly f_e vary from 1 to 10, increase with smaller A_b/σ_h, and binned-means indicate a power-law scaling. When using a spatially averaged standard deviation σ_h^{ref}, the scatter around binned-means increases, demonstrating that f_e is related to σ_h. Intercomparison with previous experiments is challenging due to different methodologies and definitions of f_e. Nevertheless, observations from multiple experiments are broadly consistent with a power-law in terms of A_b/σ_h. Given high-resolution bathymetry, our empirical f_e scaling can be used to parameterize wave dissipation over rough seabeds of coral reefs and rocky shores.

SIGNIFICANCE STATEMENT: In contrast with sandy beaches, the large seabed roughness of coral reefs and rocky shores can induce significantly larger wave dissipation by bottom friction. We present observations over a rough rocky shore, where incoming sea-swell waves are largely dissipated by bottom friction offshore of the surfzone. While theoretical expressions can estimate the wave friction factor f_e for small seabed roughness, our results provide an empirical power-law for f_e, which can be used to parameterize dissipation in wave transformation models over rough seabeds.

1. Introduction

Surface gravity waves are important drivers of nearshore processes. For example, surface gravity waves are responsible for inducing alongshore (e.g., Feddersen et al. 1998) and rip currents (e.g., Dalrymple et al. 2010), mixing and transporting material in and out of the surf zone (e.g., Moulton et al. 2023), driving sediment transport (e.g., Sherwood et al. 2022), facilitating nutrient uptake to coral reefs (Falter et al. 2004), and impacting the settlement of benthic organisms on rocky shores (Denny 1995). The impact of sea-swell waves (5–20 s wave periods) on these processes depends on nearshore wave transformation. An important wave transformation process is the wave energy dissipation induced by bottom friction D_f, which depends both on wave conditions and the roughness of the seabed (e.g., Jonsson 1966; Nielsen 1992). For waves propagating over a sandy seabed with small bed roughness, D_f is relatively weak (e.g., Thornton and Guza 1983). In contrast, enhanced wave dissipation due to the friction associated with large bed roughness has been observed on coral reefs (e.g., Lowe et al. 2005) and rocky shores (e.g., Gon et al. 2020). Therefore, accurate wave dissipation parameterizations are required to predict wave transformation over coral reefs and rocky shores.

Vertically integrated sea-swell wave dissipation D_f can be parameterized as $D_f = 0.8\rho f_e U_{\mathrm{rms}}^3$, where ρ is seawater density, U_{rms} is the root-mean-squared sea-swell wave velocity near the seabed, and f_e is the nondimensional wave energy dissipation factor (e.g., Jonsson 1966; Monismith et al. 2015, Appendix B). The parameter f_e encodes the work done by shear and drag forces (Lowe et al. 2007). Note, f_e is closely related to the wave friction factor f_w parameterizing the bottom stress in a wave boundary layer (e.g., Nielsen 1992). As $f_e \approx f_w$ is commonly assumed (Nielsen 1992), we will use the more common terminology of wave friction factor when referring to f_e.

For a rough turbulent wave boundary layer, f_e depends on A_b/k_N, the ratio of the horizontal wave orbital excursion at the seabed A_b, and bed roughness parameter k_N (Nielsen 1992). Note that for both steady and oscillatory flows k_N is not a physical distance, but is a hydraulic length scale that must be determined for each specific roughness configuration (Chung et al. 2021). In a small bed roughness regime defined as $A_b/k_N \gg 1$ (i.e., the orbital wave excursions are much larger than the bed roughness), a shear-driven turbulent boundary layer is well-defined, and k_N can be estimated by fitting observations to a logarithmic velocity profiles (e.g., Sleath 1987).

Friction factor parameterizations that assume small roughness (i.e., $A_b/k_N \gg 1$) have f_e decreasing monotonically with A_b/k_N (e.g., Jonsson 1966; Jonsson and Carlsen 1976; Grant and Madsen 1979; Madsen 1994). These f_e parameterizations have been tested in laboratory experiments of waves propagating over immobile sand grains, gravel, and rigid roughness elements on a flat bottom (e.g., Kamphuis 1975; Sleath 1987; Simons et al. 1988; Mirfenderesk and Young 2003). For immobile sand grains, k_N is proportional to the sand grain diameter, and thus $k_N \sim O(0.1\text{-}1)$ mm (e.g., Kamphuis 1974). For mobile sediment with sand ripples or bedforms with heights $O(1)$ cm, D_f can be substantially enhanced by the turbulence generated over these bedforms (Smyth and Hay 2003), implying a k_N on the scale of the ripple (e.g., Nielsen 1992). In DNS simulations of immobile sand ripples (2 cm height and 10 cm wavelength), form drag becomes more important than the viscous forces (Barr et al. 2004). Because k_N is a hydrodynamic length scale related to a shear-driven boundary layer, no methodology exists to generally determine k_N from the physical seabed geometry alone (Chung et al. 2021). For steady flows, much effort has gone into relating the roughness geometry to k_N (Flack and Schultz 2010; Rogers et al. 2018).

Wave dissipation due to bottom friction D_f is much more important on coral reefs and rocky seabeds than on sandy seabeds, due to the significantly elevated bed roughness (e.g., Monismith 2007; Gon et al. 2020; Davis et al. 2021). Several experiments have measured significant bottom-friction-induced sea-swell wave attenuation across fore-reefs in 6–15 m water depth (Hardy and Young 1996; Péquignet et al. 2011; Monismith et al. 2015; Rogers et al. 2016), reef-flats with depths < 3 m (Gerritsen 1980; Nelson 1996; Falter et al. 2004; Lowe et al. 2005; Huang et al. 2012; Lentz et al. 2016; Sous et al. 2023), and across fore-reefs with spur-and-groove formations in 5–10 m water depth (Péquignet et al. 2011; Acevedo-Ramirez et al. 2021). The vertical scale of coral reef bed roughness can be large from a few centimeters to a meter, leading to large f_e between 0.1 and 5, which are much larger than f_e on a sandy seabed.

In addition to coral reefs, rocky shores have recently been recognized as sites with potentially large bottom-friction-induced wave dissipation and can be categorized as platforms and rough rocky seabeds. Platforms can be smooth or rough, with a standard deviation of seabed elevation ranging from $O(1)$ cm to 20 cm, leading to f_e between 0.001 and 0.7 (Poate et al. 2018). On rough rocky shores, large and steep rock formations of up to several meters high can be distributed along the shoreline, in the nearshore, and throughout the continental shelf (MacMahan et al. 2024). On a rough ($O(1)$ m variability) rocky seabed, sea-swell wave attenuation between 8–6 m water depth was strong with estimated f_e between 4–34 (Gon et al. 2020).

Bed roughness k_N has been estimated on coral reefs (e.g., Rogers et al. 2016) by fitting the known f_e and A_b to an existing large A_b/k_N parameterization (e.g., Madsen 1994). The estimated bed roughness (k_N between 0.06 and 2.5 m) leads to smaller A_b/k_N (between 0.1 and 10) than on sandy seabeds. In large roughness (i.e., $A_b/k_N \leq 1$) regimes, the underlying assumptions of a traditional shear-driven turbulent wave boundary layer over flat bed break down (Chung et al. 2021). Instead, flow around canopy elements increases the energy loss due to work done by drag forces (e.g., Lowe et al. 2007; Rosman and Hench 2011; Monismith et al. 2015; Yu et al. 2018). As k_N is a hydrodynamic property that cannot be elucidated directly from observations of the rough seabed (e.g., Chung et al. 2021), how the seabed variability or geometry should be implemented in D_f parameterizations for small A_b/k_N regimes is unclear. Moreover, given differences in the relevant wave dissipation processes, the appropriate f_e over rough seabeds may not follow existing large A_b/k_N parameterizations extrapolated towards $A_b/k_N \leq 1$. Therefore, new D_f parameterizations that are based solely on quantities directly known by a wave model are required to improve wave predictions over coral reefs and rocky shores.

The standard deviation of the seabed elevation σ_h is the simplest metric of seabed variability. On coral reefs and rocky seabeds, σ_h can vary from a few centimeters (Lowe et al. 2005) to 0.9 m (Gon et al. 2020). In extrapolating f_e parameterizations developed for $A_b/k_N \gg 1$, it has been suggested that $k_N \approx 4\sigma_h$ (Lowe et al. 2005; Sous et al. 2023). Additional statistics of seabed elevation (e.g., skewness) may provide higher-order corrections to k_N (Dealbera et al. 2024). Observations of f_e, A_b, and σ_h (Lowe et al. 2005; Lentz et al. 2016; Gon et al. 2020; Sous et al. 2023) yield empirical relationships between f_e and A_b/σ_h, which are primarily based on temporally variable A_b due to the few number of locations where f_e was estimated, or limited bathymetric observations. Sous et al. (2023) estimated f_e at 3 sites that had σ_h varying between 8–15 cm, allowing some insight into the effect of variable σ_h on f_e. Yet, the impact of variable roughness on f_e has yet to be quantified.

Here, we will estimate friction factors at many locations on a rocky seabed, and we will scale observed friction factors f_e with A_b/σ_h where variable σ_h is estimated from the bathymetry. We present observations from the first ROcky shores: eXperiments and SImulations (ROXSI) experiment from the summer of 2022, which reveal strong cross-shore sea-swell wave attenuation by bottom friction. We describe the site of the experiment, the instrument array, and the data processing in Section 2. An overview of the wave conditions during the experiment indicates significant wave attenuation offshore of the surfzone (Section 3a, b). The friction factor f_e is estimated across instrument pairs from the cross-shore energy flux, and quality control criteria are applied to reduce the impact of estimation noise on f_e (Section 3c, d). The relationship between f_e and A_b/σ_h across instrument pairs is examined, where we find that f_e is partly due to the spatial variability in σ_h (Section 3e). Effects of wave direction in our estimates are discussed (Section 4a), and the observed f_e are compared with previous field measurements on coral reefs and rocky shores (Section 4b, c). We conclude with a summary of our results (Section 5).

2. Experiment description, methods, and overview of observations

a. Field site

This ROXSI field experiment took place from June 15$^{\text{th}}$ to July 21$^{\text{th}}$, 2022, on the rocky shoreline of Monterey Peninsula, California, USA (Fig. 1). Our measurements were distributed in two regions along the peninsula separated by nearly 3 km: Asilomar State Marine Reserve (Pacific Grove) and China Rock (Pebble Beach). In each region, a local cross-shore (x) and alongshore (y) right-handed coordinate system was defined where $+x$ is directed onshore. The origin of the coordinate system at China Rock (Asilomar) is at latitude 36° 36' 15.8928" N (36° 37' 26.5187" N), longitude 121° 57' 33.8134" W (121° 56' 25.1905" W), and $+x$ is directed to 105° (113°) clockwise from the geographic north.

Rough rocky shores have topography and bathymetry variability across a wide range of scales (Fig. 1b-d). The corrugated shoreline at Asilomar and China Rock have headlands and embayments at an alongshore scale of 100 meters. Rock formations, up to a few meters high, are prevalent along the coastline (Fig. 1b), and throughout the shelf where our instruments were deployed (Fig. 1c-d). The large-scale cross-shore bathymetry, i.e., across length scales much longer than the rock formations, has a relatively large slope of 1:40.

The rocky morphology changes primarily on geological timescales such that multiple datasets can be combined to map the bathymetry. For water depths typically deeper than 10 m, historical multibeam data gridded at 2 m resolution is available from the California State University, Monterey Bay (CSUMB, Seafloor Mapping Lab 2014). The multibeam bathymetry has an uncertainty in the vertical elevation of ± 5 cm^{-1} (Barnard et al. 2011). At shallower water, data comes primarily from bathymetric lidar by the Joint Airborne Lidar Bathymetry Technical Center of Expertise (JALBTCX). The point cloud lidar data has an irregular spatial distribution, with a typical spacing of 0.5 to 2 m between data points, where the individual point error is $\sim$ 15 cm (OCM Partners 2024). The bathymetry at depths shallower than about 10 m was also mapped with an echosounder and a survey-grade GPS mounted on a Rotinor DiveJet underwater scooter that is operated at the sea surface. The echosounder is a feature of the Nortek Signature1000 Acoustic Doppler Current Profiler (ADCP) mounted at the front of the DiveJet, and this system yields bottom depth data at sub-meter resolution along surveyed tracks. The gridded bathymetry was computed by averaging elevations relative to mean sea level z_{msl} within 2 m by 2 m boxes in (x, y), and we refer to the water depth as $\overline{h} = -z_{\mathrm{msl}}$.

b. Bottom roughness

Throughout this paper, we characterize the seabed roughness with the standard deviation of bottom depth $\sigma_h(x, y)$ (Fig. 2). The ungridded bathymetric elevations within 20 m by 20 m boxes were used to compute σ_h at 2 m resolution. Elevations in each box were first detrended with a plane fit, and the standard deviation σ_h was computed as the root-mean-squared of detrended bottom depth within each box. Our choice for the 20 m length scale is based on a trade-off between statistical reliability of σ_h and resolving spatial variability of σ_h between our instrument sites, where the typical cross-shore spacing is between 30 and 70 m. Regions with low concentration of bathymetry data have 0.5 elevation data points per square meter, such that σ_h is computed from at least 200 data points. Given the box size, the longest horizontal length scale included in σ_h is 20 m. Given the data density, σ_h represents variability longer than 1–4 m depending on the location and data density.

As expected from the rocky morphology (Fig. 1c), large σ_h are observed at our study site (Fig. 2). The spatially averaged σ_h at China Rock and Asilomar are 0.81 and 0.62 m, respectively. In terms of the 10% and 90% quantiles, σ_h ranges from 0.42 m and 1.18 m at China Rock, and 0.19 m and

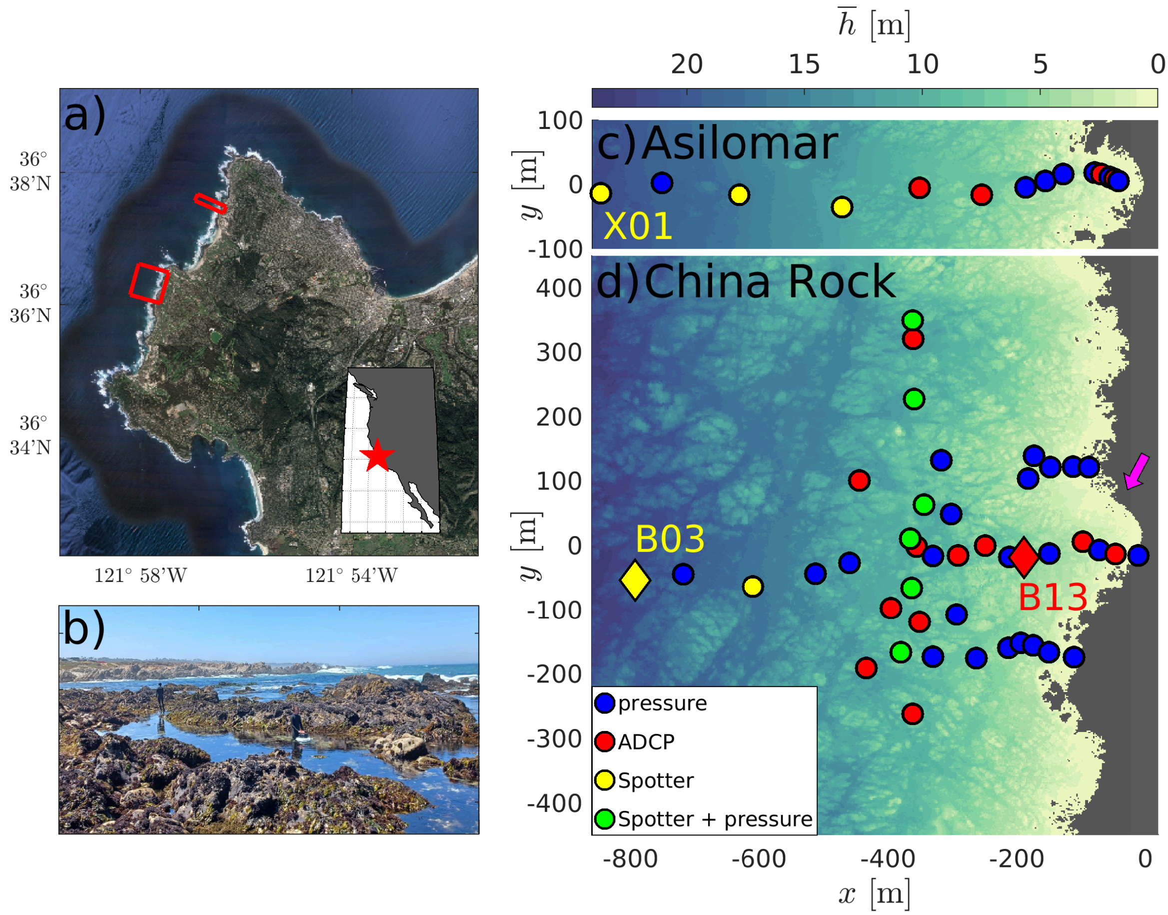

Fig. 1. Study site bathymetry and instrument array: (a) Monterey Peninsula, California, USA (the inset shows the location of the peninsula along the west coast of North America). Red rectangles in (a) show the location of the instrument arrays at Asilomar and China Rock. (b) Photograph of the rocky shoreline at China Rock. Water depth relative to mean sea level ($\overline{h}$) with overlaid instrument arrays at (c) Asilomar and (d) China Rock, as functions of local cross-shore x and alongshore y coordinates. Dots are colored by type of measurement: pressure sensors (blue), ADCPs (red), Spotter wave buoys (yellow), and Spotters with co-located pressure sensors (green). Instrument locations B03 and B13 (diamonds) are used in Figs. 3 and 4.

1.00 m at Asilomar. These statistics quantify the smaller bottom roughness at Asilomar, which is partly due to wide sandy patches with low σ_h (e.g., at $(x, y) = (-400$ m, 25 m$)$ in Fig. 2a), and partly due to smaller rocks than at China Rock. The σ_h in our study sites is larger than on coral reefs, where σ_h typically varies from 2 to 20 cm (Lowe et al. 2005; Nunes and Pawlak 2008; Amador et al. 2020; Sous et al. 2023). The larger σ_h in our study site is consistent with results from MacMahan et al. (2024), where bathymetry data from several coral reefs and rocky shores indicate the average σ_h on the latter is three times larger.

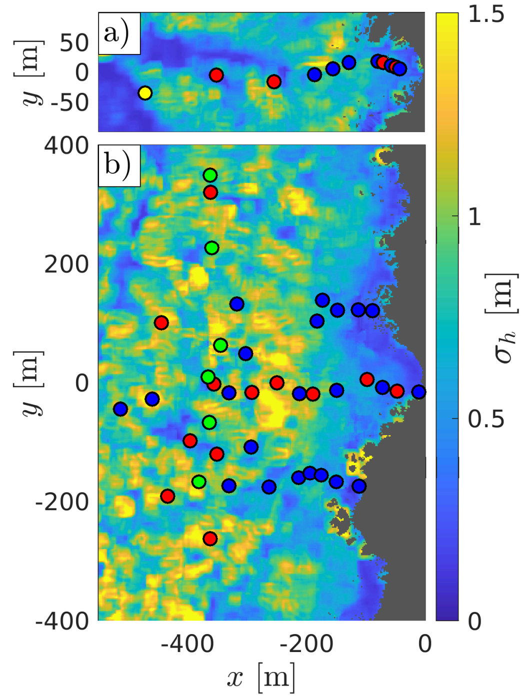

FIG. 2. Maps of the standard deviation of bottom depth σ_h as a function of local cross- (x) and alongshore (y) coordinate systems at (a) Asilomar and (b) China Rock. Dots denote instrument locations as in Fig. 1.

c. *Instrument array and data processing*

We deployed instrument arrays off Asilomar, Pacific Grove within the Asilomar State Marine Reserve, and off China Rock, Pebble Beach (Fig. 1c, d), between June 15$^{\text{th}}$ and July 21$^{\text{th}}$, 2022. The instrument array at Asilomar is an approximate cross-shore transect from $\overline{h} = 21$ m to $\overline{h} = 2$ m extending off a small embayment, where instruments at shallower water ($x > -100$ m in Fig. 1c) were deployed within a deeper channel along the northern half of the embayment. The more extensive array at China Rock consists primarily of 3 cross-shore transects (at $y = -200$ m, $y = 0$ m, and $y = 100$ m) with additional instruments deployed in the alongshore for $6 \leq \overline{h} \leq 14$ m.

This paper focuses on sea-swell wave-resolving observations from wave buoys, Acoustic Doppler Current Profilers (ADCPs), and pressure sensors. Wave buoys were deployed at water depths of 10 m or deeper, and most ADCPs and pressure sensors were deployed in $\overline{h} \leq 10$ m. Sofar Spotter wave buoys (Herbers et al. 2012; Raghukumar et al. 2019), which provide GPS-based vertical and horizontal sea surface displacements at a sampling rate of 2.5 Hz, were deployed for $\overline{h} \geq 10$ m. The wave buoys distributed in the alongshore around $\overline{h} \approx 10$ m at China Rock were directly cabled to bottom-mounted RBR Coda pressure sensors measuring at 2 Hz. Additional near-bottom pressure measurements were made by either RBR soloDs or internal pressure sensors from ADCPs at sampling rates between 2 and 8 Hz. We subtracted the atmospheric pressure from our pressure data based on measurements at the Monterey Harbor ($\approx$ 6 km from our instrument arrays) by the National Oceanic and Atmospheric Administration.

Sea-surface elevation spectra $S_\eta(f)$, where f is the frequency, are directly computed from vertical displacements measured by wave buoys. We computed hourly spectra using 120 s-long segments with 50% overlap and tapered with a Hanning window. The resulting frequency resolution is approximately 0.008 Hz with 118 degrees of freedom. Pressure spectra $S_p(f)$ are calculated in the same manner and are converted to $S_\eta(f)$ via

$$S_\eta = K^2 S_p, \tag{1}$$

where S_p is the spectra calculated from pressure in units of meters (converted from Pa by normalizing with $\rho_0 g$, where $\rho_0 = 1025\ \mathrm{kg\,m^{-3}}$, and gravitational acceleration $g = 9.8\ \mathrm{m\,s^{-2}}$), and K is the transfer function from linear wave theory

$$K = \frac{\cosh(kh)}{\cosh(k z_{\mathrm{hab}})}, \tag{2}$$

where k is the wavenumber, h is the water depth, and z_{hab} is the height above the bottom of the pressure measurement (e.g., Guza and Thornton 1980; Bishop and Donelan 1987). The wavenumber was estimated from the dispersion relationship of linear surface gravity waves, i.e.

$$\omega^2 = gk \tanh(kh), \tag{3}$$

where ω is the radian wave frequency ($\omega = 2\pi f$).

The flat-bottom approximation assumed in (2) leads to errors in estimates of significant wave heights from pressure sensors (Marques et al. 2024). Co-located instruments in the China Rock array around $\overline{h} = 10$ m show that pressure sensors consistently overestimate the significant wave height from wave buoys when (2) is evaluated at the local depth measured by a pressure sensor. When evaluating (2) with a spatially averaged water depth within a radius $r = 13$ m of each pressure sensor, errors in pressure-based wave heights errors are reduced to ± 10 % from wave buoys. We followed the approach outlined in Marques et al. (2024) and calculated a depth correction to the pressure sensor observations based on the mean water depth around each instrument, where the averaging r decreases towards shallower water. Alternatively, we also estimated wave statistics using the local water depth at each pressure sensor to address the sensitivity of our results. Friction factor estimates using either the local or the spatially averaged depth are typically within 20% of each other.

From the sea-surface elevation spectrum, we computed hourly estimates of the sea-swell significant wave height

$$H_s \equiv 4\sqrt{\int_{\mathrm{SS}} S_\eta(f)\,\mathrm{d}f}, \tag{4}$$

where the subscript SS under the integral sign denotes the sea-swell (0.05–0.2 Hz) frequency band. The high-frequency cut-off prevents overestimates of H_s from S_η contaminated at higher frequencies, where noise overwhelms a small wave-induced pressure variance. Moreover, wave buoy estimated wave energy at $f > 0.2$ Hz and $f < 0.05$ Hz was relatively small in our experiment. Additional hourly sea-swell bulk statistics include mean period T_{mean}, and mean direction θ_{mean} (see definitions in Appendix A).

We will estimate sea-swell energy dissipation by bottom friction and wave friction factors, which depend on the near-bed root-mean-square (rms) orbital wave velocity U_{rms} (e.g., Monismith et al. 2015)

$$U_{\mathrm{rms}} = \sqrt{\int_{\mathrm{SS}} \left(\frac{2\pi f}{\sinh(kh)}\right)^2 S_\eta(f)\,\mathrm{d}f} \tag{5}$$

and the horizontal orbital excursion

$$A_b = \sqrt{2\int_{\mathrm{SS}} \frac{1}{\sinh(kh)^2} S_\eta(f)\;\mathrm{d}f}. \tag{6}$$

The $\sqrt{2}$ factor relates the root-mean-squared variability of the horizontal orbital excursion to a scale A_b for the amplitude of the corresponding orbital excursion.

d. Energy balance equation

Numerical wave models typically solve the wave action conservation equation to predict the evolution of the wave spectrum (e.g., Booij et al. 1999). In the absence of wave-current interaction, wave action conservation simplifies to the wave energy conservation equation. We consider the sea-swell frequency-band integrated energy equation,

$$\frac{\partial E}{\partial t} + \frac{\partial F_x}{\partial x} + \frac{\partial F_y}{\partial y} = -D_b - D_f, \tag{7}$$

where E is the wave energy density, F_x and F_y are the cross-shore and alongshore components of the bulk (frequency-integrated) energy flux, D_b is wave dissipation by depth-limited wave breaking, and D_f is the wave dissipation by bottom friction. Infragravity wave energy in our study site is very weak relative to sandy beaches (at most 1 % of sea-swell wave energy), and thus we neglect nonlinear triad interactions that can transfer energy from the latter into the infragravity band on sandy shorelines (Herbers et al. 1994). Energy input from the wind is also neglected. Sous et al. (2023) determined that including wave-current interaction only weakly affected the estimated friction factor. The strength of wave-current interaction is given by the nondimensional parameter U/c where U is the depth-averaged mean current scale and c is the wave phase speed. In Sous et al. (2023), this parameter was ≤ 0.1. Similarly, this parameter is also < 0.1 for our observations (not shown) justifying neglecting wave-current interaction. The components of the bulk energy flux are,

$$F_x = \int_{\mathrm{SS}} \rho_0 g a_1(f) S_\eta(f) c_g(f)\, \mathrm{d}f, \tag{8a}$$

$$F_y = \int_{\mathrm{SS}} \rho_0 g b_1(f) S_\eta(f) c_g(f)\, \mathrm{d}f, \tag{8b}$$

where $a_1(f)$ and $b_1(f)$ are the first directional moments (Appendix A) and

$$c_g(f) = c_p(f)\frac{1}{2}\left[1 + \frac{2kh}{\sinh(2kh)}\right] \tag{9}$$

is the group velocity, and c_p is the phase speed $c_p = \omega/k$.

Here, we seek to estimate the bottom-friction-induced wave dissipation D_f. In principle, the left-hand side of (7) can be applied to observations from instrument arrays to measure the total wave dissipation on the right-hand side. In practice, additional assumptions are required to simplify (7) and estimate D_f from instrument arrays. The unsteady term $\partial E/\partial t$ can be readily evaluated, and this term is negligible at all locations where significant wave dissipation was observed. Moreover, directional fluxes (8) can only be estimated where ADCPs and Spotter wave buoys were deployed (Fig. 1c, d), which substantially decreases the number of instrument pairs for estimating wave dissipation. However, assuming negligible reflection and small angle of incidences, $a_1 \approx 1$, $b_1 \approx 0$, (8) is approximated to

$$F_x \approx F = \int_{\mathrm{SS}} \rho_0 g S_\eta(f) c_g(f)\, \mathrm{d}f, \tag{10a}$$

$$F_y \approx 0. \tag{10b}$$

This approximation allows the energy flux F to be computed for all stand-alone pressure sensors, and the wave dissipation can be computed between a larger number of instrument pairs from (10a). Onshore wave propagation with small reflection are widely used assumptions assumed to measure convergences of F from pressure sensors (e.g., Monismith et al. 2015; Lentz et al. 2016; Sous et al. 2023). If the water depth is sufficiently deep where depth-limited wave breaking can be neglected, then $D_b = 0$ and the wave dissipation can be assumed to be entirely due to bottom friction D_f (e.g., Monismith et al. 2015). Taking all these approximations into account, we rewrite (7) as

$$\frac{\mathrm{d}F}{\mathrm{d}x} = -D_f + \epsilon, \tag{11}$$

where ϵ represents all the neglected processes, which can be considered as noise in the estimates of D_f and friction factor f_e.

3. Results

a. Overview of sea-swell wave conditions

Sea-swell wave statistics observed in our 40-day experiment were characteristic of summer mild wave conditions on the Monterey Peninsula. From our offshore wave buoy at China Rock deployed at $\overline{h} = 21$ m (B03 in Fig. 1c), H_s varied from 0.3 to 2.0 m and and T_{mean} varied from 5.8 to 11.4 s (Fig. 3a, b). Larger wave heights were mostly associated with incident waves from the northwest ($\theta_{\mathrm{mean}} < 0$ in Fig. 3c) and the experiment-averaged mean period is $T_{\mathrm{mean}} = 7.9$ s. Longer period waves from the southwest ($\theta_{\mathrm{mean}} > 0$) tended to have smaller wave heights. Incident θ_{mean} at B03 rarely exceeded 20° and the 20% and 80% percentiles were -11.9° and 7.4° (Fig. 3c).

A substantial decrease in H_s is observed between the offshore wave buoy and measurements taken at $\overline{h} \approx 5$ m (instrument site B13, Fig. 3a). The reduction in H_s is about 0.1-0.3 m (15-25%) and occurs in deeper water depths than where depth-limited wave breaking is expected. For a saturated surfzone with $\gamma = H_s/h = \sqrt{2}\times 0.45 \approx 0.6$ (e.g., Thornton and Guza 1982), depth-limited breaking for the most energetic wave events in the experiment ($H_s \approx 2$ m) is expected to be important at water depths less than 3.5 m, which is shallower than $\overline{h} = 5$ m at B13. Although the bathymetry is rough and the water depth does not vary monotonically in the cross-shore, the smallest water depths offshore of B13 are $\overline{h} \approx 4$ m, and depth-limited wave breaking can not account for the observed decrease in H_s between B03 and B13. The mean period T_{mean} is nearly conserved across instrument sites, and the smaller magnitude of θ_{mean} at shallower water indicates that sea-swell waves become more normally incident as they propagate onshore. The conserved T_{mean} and the changes in θ_{mean} qualitatively agree with the sea-swell wave transformation expected from linear

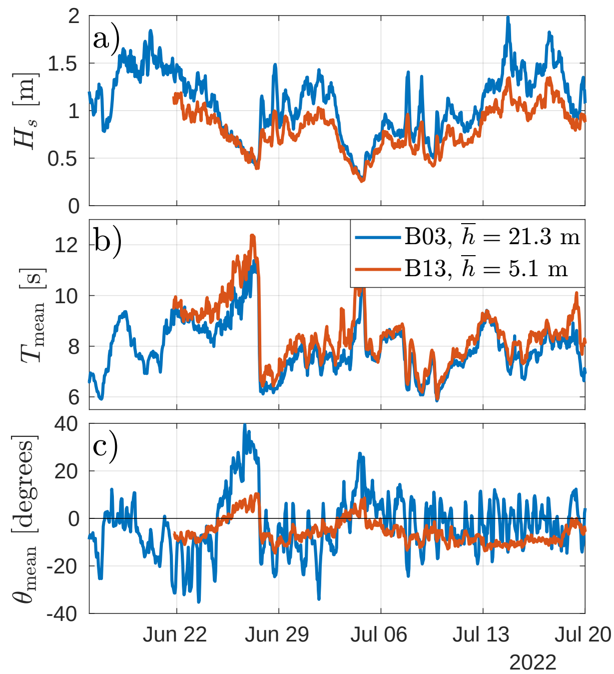

Fig. 3. Timeseries of (a) significant wave height H_s, (b) mean period T_{mean}, (c) mean wave direction θ_{mean} at instrument sites B03 and B13 (diamonds in Figs. 1 and 4). Sea-swell wave statistics were computed between 0.05 and 0.2 Hz (Section 2c). Time mean water depths $\overline{h}$ at B03 and B13 are 21 and 5 m, respectively. Positive (negative) θ_{mean} indicates waves from the southwest (northwest).

wave theory with no wave dissipation (Herbers et al. 1999), while the observed decrease in H_s does not (e.g., Dean and Dalrymple 1991).

b. Cross-shore wave attenuation

Experimental time-mean sea-swell wave statistics across the instrument array further highlight the attenuation of sea-swell waves at water depths well seaward of the surfzone (Fig. 4). Most instrument locations at $\overline{h} > 8$ m have smaller time-mean H_s than observed offshore, and the average H_s decrease across these instruments is 5% (Fig. 4a). Time-mean wave height further decreases towards shallower instruments at $\overline{h} \approx 3$ m. We next examine the cross-shore evolution of the normalized wave energy flux F/F_0 (Figure 4b) where F_0 is the most offshore wave energy flux estimated at either B03 or X01 for China Rock or Asilomar, respectively. As the wave energy flux is proportional to H_s^2 and the group velocity decreases shoreward of $\overline{h} < 15$ m (for the time-averaged mean period $T = 7.9$ s), a pronounced decrease in F/F_0 is also observed seaward the surfzone (Fig. 4b). For $\overline{h} \leq 8$ m, the time-mean flux consistently decays towards shallower water, and F/F_0 is close to 0 at $\overline{h} = 2$ m. For $8 \leq \overline{h} \leq 13$ m, overall time-mean F/F_0 is mostly < 1. Spatial

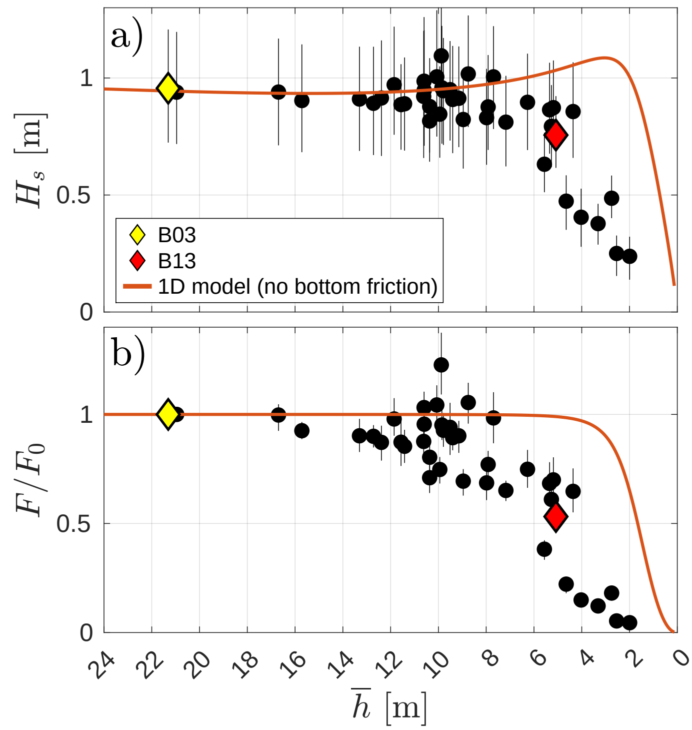

FIG. 4. Cross-shore transformation of sea-swell wave statistics as a function of mean depth $\overline{h}$: (a) significant wave height H_s and (b) normalized energy flux F. Energy flux is normalized by the offshore value either at B03 or X01 for China Rock or Asilomar, respectively. Symbols are experiment averages, and vertical bars show 25% and 75% percentiles. Diamonds show observations that are also discussed in Fig. 3, and their location is shown in Fig 1c. The orange line is the H_s and the energy flux F predicted by integrating a 1D energy balance equation (11) developed for sandy shores (Thornton and Guza 1983) using the time-mean $\overline{H}_s = 1$ m and $\overline{T}_{\text{mean}} = 7.9$ s .

variability in F/F_0 is potentially due to wave focusing and defocusing over the spatially variable bathymetry across the entire array. Although wave reflection at the site is weak (3–6%, Collins et al. 2024b), it may influence the spatial variability in F/F_0.

The observed H_s and F/F_0 have large differences from the expected wave statistics on sandy beaches (Fig 4). Sea-swell wave transformation on sandy beaches is well-described by a simple cross-shore model (e.g., Thornton and Guza 1983; Ruessink et al. 2001) between energy flux divergence and dissipation by wave breaking. Assuming a narrow-band wave field, Rayleigh-distributed wave heights, and a parameterization for wave breaking in a saturated surfzone, the energy equation can be integrated to yield the cross-shore profiles of significant wave height and energy flux (e.g., Thornton and Guza 1983). Dissipation by wave breaking was parameterized following Thornton and Guza (1983), with their standard wave breaking parameters $\gamma = 0.45$ and $B = 1$. To contrast our time-mean observations with what is expected for a sandy beach, we integrated the energy equation for a linearly sloping beach with a 1:40 slope, normally incident waves, and wave height and mean period that matches the statistics in our offshore observations (i.e. $\overline{H}_s = 1$ m and $\overline{T} = 7.9$ s). The modeled F/F_0 is essentially constant for $\overline{h} \geq 5$ m and decreases $< 10\%$ until $\overline{h} = 3$ m (figure 4b). The modeled wave height increases between $6 \leq \overline{h} \leq 3$ m m, consistent with the nearly conserved F, before rapidly decreasing at water depths shallower than $\overline{h} = 2.5$ m due to wave breaking (Fig. 4a). In the range of 13–5 m water depth where wave breaking is not occurring, the modeled F and H_s are at the upper limit of the observations, indicating that non-breaking processes are leading to the decay in the observed wave energy flux.

c. Estimation of the friction factor

The rough bathymetry at our study site (Fig. 2) and the large sea-swell attenuation seaward the surfzone (Fig. 4) suggest that energy dissipation by bottom friction is a dominant term in the energy balance. Sea-swell wave dissipation by bottom friction can be parameterized (Appendix B) by a friction factor f_e through

$$D_f = 0.8\rho f_e U_{\mathrm{rms}}^3. \tag{12}$$

We test the hypothesis that dissipation is due to bottom friction by assuming the energy balance

$$\frac{\mathrm{d}F}{\mathrm{d}x} = -D_f. \tag{13}$$

Substituting (12) into (13) yields

$$f_e = -\frac{\mathrm{d}F}{\mathrm{d}x}\frac{1}{0.8\rho U_{\mathrm{rms}}^3}. \tag{14}$$

To estimate f_e from our observations, hourly energy flux convergence $-\mathrm{d}F/\mathrm{d}x$ was computed with a finite difference between adjacent cross-shore instruments. The instrument arrays at China Rock and Asilomar have 33 pairs of adjacent instruments that are roughly aligned in the cross-shore. The U_{rms} used in (14) was the mean between the two instrument locations, which we denote by $\langle U_{\mathrm{rms}}\rangle$, and then cubed $\langle U_{\mathrm{rms}}\rangle^3$ for computing f_e (as in Monismith et al. 2015). Moreover, a bulk friction factor $\tilde{f}_e$ was computed from the least-squares fit between $\langle U_{\mathrm{rms}}\rangle^3$ and $-\mathrm{d}F/\mathrm{d}x$, which is a proxy for the time-averaged friction factor and has less uncertainty than hourly estimates of f_e.

As an example of the f_e estimation, we show observations from one pair of instruments (B11–B12), where energy flux convergence was measured and it has an excellent agreement with the parameterized dissipation D_f (Fig. 5). Instrument locations B11 and B12 were separated by $\Delta x \approx 40$ m in the cross-shore, by $\Delta y \approx 18$ m in the alongshore, and the time-mean water depths $\overline{h}$

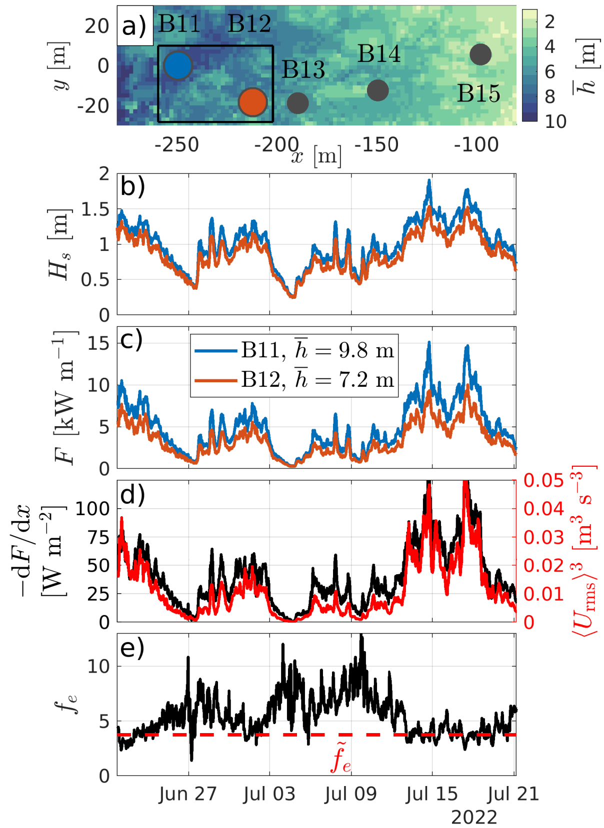

FIG. 5. Example of the estimation of f_e. (a) Bathymetry map around instrument locations B11–B15 (where the rectangle is used to compute $\langle \sigma_h \rangle$ in Fig. 6). Time series of wave statistics and friction factor estimates from B11 (blue lines) and B12 (orange lines) locations: (b) Significant wave height H_s; (c) Energy flux F; (d) Energy flux convergence $-\mathrm{d}F/\mathrm{d}x$ (black) and the cube of the sea-swell root-mean-squared seabed orbital velocity averaged between both sites $\langle U_{\mathrm{rms}} \rangle^3$ (red); and (d) hourly friction factor f_e (14) and the bulk friction factor $\tilde{f}_e$. The correlation coefficient squared between $-\mathrm{d}F/\mathrm{d}x$ and $\langle U_{\mathrm{rms}} \rangle^3$ is $r^2 = 0.91$.

were 9.8 and 7.2 m (Fig. 5a). A small but consistent decrease in H_s is observed between instruments (Fig. 5b), and the difference in time-mean $\overline{H_s}$ is 13 cm (13%). The attenuated wave height leads to a decrease in F (Fig. 5c) and a time-average energy flux convergence $-\overline{\mathrm{d}F/\mathrm{d}x} = 38$ W m^{-2} (Fig. 5d). The energy flux convergence is highly correlated with $\langle U_{\mathrm{rms}} \rangle^3$, which yields squared correlation $r^2 = 0.91$ and supports that dissipation is well-represented by bottom friction and the assumptions within (12) and (13). The resulting f_e varies between 2 and 12 throughout the experiment, which tends to decrease with increasing H_s, and the bulk friction factor is $\tilde{f}_e = 3.7$.

d. Quality Control of Instrument Pairs

The observations from the ROXSI experiment provide an unprecedented number of instrument locations to estimate f_e in a single study site. However, unlike the results from instrument pair B11–B12, D_f may be small at other locations and the energy flux balance may not be well-represented by (12) and (13). To ensure reliable friction factor estimates, we applied quality control criteria to the analysis of the observations. The first category of quality control criteria applies to the spacing of adjacent instrument pairs. The cross-shore separation (Δx) of instrument pairs is required to be in the range $20 \leq \Delta x < 120$ m. Very short instrument separation can lead to large noise in $\mathrm{d}F/\mathrm{d}x$ and subsequently noisy estimates of f_e. The large Δx cut-off criterion eliminates pairs where the finite difference approximation of $\mathrm{d}F/\mathrm{d}x$ and the spatial average of $\langle U_{\mathrm{rms}} \rangle^3$ in (14) are inaccurate to estimate f_e. Second, the alignment of adjacent instruments can substantially depart from being cross-shore oriented. Thus, we require instrument pairs to have $|\Delta y/\Delta x| < \tan(30°)$, where Δy is the alongshore instrument separation. These two quality control criteria remove 13 out of a total of 33 adjacent instrument pairs.

The second quality control category applies to time-dependent variables. As negative friction factor is unphysical, f_e are only estimated for positive energy flux convergence ($-\mathrm{d}F/\mathrm{d}x > 0$), and we removed times when $-\mathrm{d}F/\mathrm{d}x < 0$. Bulk $\tilde{f}_e$ estimated without this constraint are very similar (typically within 1%) to those estimated with the constraint, indicating weak bias. We also removed times when either an instrument in the pair has $h < 2$ m (which may occur at low tide), since the large seabed roughness for such shallow bathymetry can lead to outcropping rocks, near which wave transformation can significantly depart from the one-dimensional balance (13). Since (12)-(14) neglect wave breaking, we applied a criterion on the ratio of H_s to h to neglect observed energy flux convergence due to wave breaking. Depth-limited wave breaking approximately begins when $H_s/h > \gamma$, where γ is often taken as 0.6 (Thornton and Guza 1982), but observations on sandy beaches can vary between 0.4 to 0.8 (e.g., Sallenger and Holman 1985). We require that $H_s/h < 0.25$ as a conservative criterion to ensure that wave breaking is not contaminating the f_e estimates. Times when $H_s/h \geq 0.25$ at any instrument were removed. If either time series across an instrument pair has more than 20% of data that do not pass any quality control criterion, then the corresponding instrument pair is removed. These criteria result in the removal of five additional instrument pairs, yielding 15 instrument pairs that satisfy what we denote as the primary quality control criteria. Given both the deployment of each instrument and the quality control criteria, the average length of the timeseries across these 15 instrument pairs is 27.4 days, with minimum and maximum lengths of 23.25 and 34 days.

Statistics from the 15 instrument pairs that pass primary quality control criteria are examined in Table 1, where pairs from $N = 1$ to $N = 15$ are sorted for decreasing r^2. Our estimates of f_e

TABLE 1. Statistics of instrument pairs that passed primary quality control criteria. Cross-shore and alongshore instrument separations are denoted by Δx and Δy. The experiment-averaged (denoted by an overbar) of $\overline{H}_s$, $\overline{U}_{\mathrm{rms}}$, and $\overline{A}_b$ are shown at each location for all instrument pairs. The mean water depth between instrument sites is denoted by $\langle \overline{h} \rangle$. The correlation coefficient squared r^2 is computed between $-\mathrm{d}F/\mathrm{d}x$ and $\langle U_{\mathrm{rms}} \rangle^3$. The bulk friction factor $\tilde{f}_e$ is given by a least-squares fit between $-\mathrm{d}F/\mathrm{d}x$ and $\langle U_{\mathrm{rms}} \rangle^3$. The spatially averaged standard deviation of bed elevation is given by $\langle \sigma_h \rangle$. Results are presented for decreasing r^2.

N	ID	$\langle \overline{h} \rangle$ [m]	Δx [m]	Δy [m]	$\overline{H}_s$ [m]	$\overline{U}_{\mathrm{rms}}$ [m s^{-1}]	$-\overline{\mathrm{d}F/\mathrm{d}x}$ [W m^{-2}]	r^2	$\tilde{f}_e$	$\overline{A}_b$ [m]	$\langle \sigma_h \rangle$ [m]
1	B11-B12	8.5	38	-18	1.00-0.86	0.19-0.21	40	0.92	3.8	0.45-0.50	1.11
2	E03-D01	9.0	102	-10	1.19-0.89	0.23-0.20	32	0.88	2.9	0.48-0.44	0.77
3	X08-X09	4.3	27	11	0.56-0.48	0.18-0.17	13	0.86	1.6	0.43-0.40	0.84
4	B14-B15	4.2	52	18	0.65-0.50	0.19-0.22	19	0.86	2.3	0.45-0.52	0.63
5	X07-X08	5.0	31	10	0.87-0.53	0.25-0.17	63	0.81	5.1	0.52-0.40	0.96
6	B12-B13	6.1	22	-1	0.87-0.81	0.21-0.25	35	0.81	2.7	0.50-0.59	1.04
7	X09-X10	3.3	49	2	0.50-0.33	0.17-0.15	13	0.80	2.1	0.40-0.37	0.69
8	X06-X07	7.2	68	12	0.96-0.84	0.19-0.24	20	0.76	1.5	0.40-0.50	0.62
9	B13-B14	5.3	40	7	0.79-0.67	0.24-0.19	17	0.71	1.4	0.59-0.46	0.86
10	A02-A04	7.0	68	-2	1.11-0.99	0.25-0.26	20	0.65	1.0	0.53-0.55	0.72
11	A01-E05	9.9	54	25	1.02-0.93	0.17-0.21	22	0.64	2.4	0.36-0.46	1.08
12	B05-B06	15.0	95	36	1.00-0.95	0.13-0.15	7	0.59	2.3	0.32-0.36	0.55
13	B09-B10	10.0	39	1	1.08-1.03	0.20-0.20	15	0.59	1.3	0.45-0.44	0.96
14	E09-D02	10.8	42	-14	0.98-0.91	0.18-0.16	13	0.43	1.8	0.43-0.36	0.99
15	B15-B16	3.0	26	-13	0.50-0.41	0.22-0.16	8	0.36	1.1	0.52-0.40	0.53

span a wide range of water depths, where the mean depth between instrument sites in each pair $\langle \overline{h} \rangle$ varies from near 3 m to 17 m. The cross-shore instrument spacing Δx is between 26 and 102 m, and most (10) instrument pairs have $|\Delta y/\Delta x| < \tan(20°)$. The time-mean $\overline{H}_s$ decreases towards shallower water across instrument pairs, on average by 0.13 m, indicating wave dissipation by bottom friction. The overall decrease in wave energy flux yields an inferred time-mean wave dissipation $-\overline{\mathrm{d}F/\mathrm{d}x}$ ranging from 8–63 W m^{-2} across instrument sites, with an average of 23 W m^{-2}. The observed time-mean $\overline{U}_{\mathrm{rms}}$ and $\overline{A}_b$ vary across instrument within 0.13–0.26 m s^{-1} and 0.32–0.59 m, respectively. For each instrument pair in Table 1, $\overline{U}_{\mathrm{rms}}$ and $\overline{A}_b$ can increase onshore due to the effect of decreasing water depth in (5) and (6).

For the 15 locations that passed primary quality control, we next examine the squared correlation coefficients r^2 between $-\mathrm{d}F/\mathrm{d}x$ and $\langle U_{\mathrm{rms}} \rangle^3$, a metric for how well the simple wave energy balance (13) holds. If terms neglected in (13) are also important or if $-\mathrm{d}F/\mathrm{d}x$ is too noisy, then r^2 should be small. In contrast, a high r^2 supports that the underlying assumptions in (12)-(14) are valid, implying accurate hourly estimates of f_e. The squared correlation r^2 varies from 0.92 to 0.36 (Table 1), and is generally higher with larger $-\overline{\mathrm{d}F/\mathrm{d}x}$, which suggests that (13) is a more accurate leading-order balance of the energy balance where dissipation is stronger. Overall, shallower water depths $\langle\overline{h}\rangle < 10$ m tend to have larger $-\overline{\mathrm{d}F/\mathrm{d}x}$ and r^2 (Table 1). For $\langle\overline{h}\rangle \geq 10$ m, the r^2 of 0.43–0.64 are amongst the lowest, indicating that other terms not included in (13) are non-negligible at these depths, and that f_e is less reliable. Across the 15 locations, the bulk friction factor $\tilde{f}_e$ ranges from 1.1 to 5.1, with an average of 2.2 across the sites. Our observed $\tilde{f}_e > 1$ are comparable to the largest estimates of the friction factor reported at very rough coral reefs (Monismith et al. 2015; Rogers et al. 2016; Lentz et al. 2016; Sous et al. 2023) and rocky seabed (Gon et al. 2020).

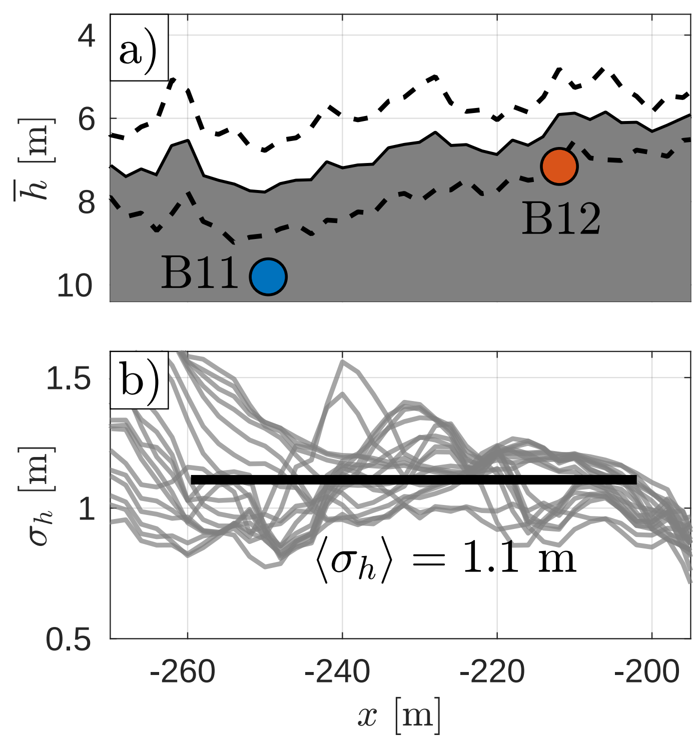

FIG. 6. (a) Alongshore-averaged $\overline{h}$, within the same bounds as the rectangle in Fig. 5a, where the dashed lines denote the averaged depth plus or minus 1 standard deviation (computed from the alongshore distribution of $\overline{h}$). (b) Cross-shore profiles of the standard deviation of bottom depth σ_h (grey lines), where the black line is the mean of σ_h within the rectangle in Fig. 5a. Blue and orange circles in (a) denote the locations in the cross-shore and in the vertical of instruments at locations B11 and B12.

The seabed roughness for each instrument pair that passed the quality control criteria was computed as the spatially averaged standard deviation of seabed elevation $\langle\sigma_h\rangle$. The gridded σ_h was averaged within a rectangle bounding instrument locations for each pair in Table 1 (e.g., see Fig. 5a for pair $N = 1$). As an example, the large bottom depth variability around instrument pair

B11–B12 is associated with σ_h between 0.8 m and 1.7 m (Fig. 6). Note that variations in σ_h across horizontal scales shorter than ≈ 10 m are relatively small because σ_h was computed within 20 m by 20 m boxes (Section 2b). The bathymetry around instruments B11 and B12 yields the largest $\langle\sigma_h\rangle$ across all instrument pairs, where $\langle\sigma_h\rangle$ varies between 0.53 m and 1.11 m (Table 1).

e. Dependence of f_e on A_b/σ_h

The dependence of f_e on A_b/σ_h is now addressed with the first 10 instrument pairs in Table 1 that have $r^2 \geq 0.65$. Both A_b and σ_h are averaged between instrument locations resulting in $\langle A_b\rangle$ and $\langle\sigma_h\rangle$. For these instrument pairs, the mean (time and across pairs) of $\langle A_b\rangle$ is 0.5 m. The mean of $\langle\sigma_h\rangle$ is $\sigma_h^{\mathrm{ref}} = 0.8$ m, with a standard deviation of 0.2 m. The observed hourly f_e are large, typically between 1 and 10, and consistently decrease with $\langle A_b\rangle/\langle\sigma_h\rangle$ that varies between 0.2–1 (gray dots in Fig. 7a). The correlation coefficient squared r_*^2 between the hourly $\log_{10}(f_e)$ and $\log_{10}(\langle A_b\rangle/\langle\sigma_h\rangle)$ is $r_*^2 = 0.43$ (Fig. 7a), suggesting a power-law relationship, albeit with scatter. In terms of the 25% and 75% quartiles within each $\langle A_b\rangle/\langle\sigma_h\rangle$ bin, the ratio between the upper and lower f_e quartile is about 2. In log space, the bin-averaged f_e (black dots in Fig. 7a) has a very clear linear relationship with $\langle A_b\rangle/\langle\sigma_h\rangle$, further indicating a power-law relationship.

Given the variable $\langle\sigma_h\rangle$ and the large number of instrument pairs with f_e estimates, we assess whether f_e is as effectively scaled with a uniform σ_h^{ref} by examining the f_e and $\langle A_b\rangle/\sigma_h^{\mathrm{ref}}$ relationship (Fig. 7b). Overall the relationship is qualitatively similar to that with $\langle A_b\rangle/\langle\sigma_h\rangle$ because f_e is largely explained by temporal variability in $\langle A_b\rangle$. However, the resulting $r_*^2 = 0.28$ is substantially lower than the $r_*^2 = 0.43$ for $\langle A_b\rangle/\langle\sigma_h\rangle$. These two r_*^2 are distinct as the 95% confidence level is near ± 0.02 (Emery and Thomson 2014). The binned-mean f_e versus $\langle A_b\rangle/\sigma_h^{\mathrm{ref}}$ reveal a less consistent power-law relationship than for $\langle A_b\rangle/\langle\sigma_h\rangle$. The 25%-75% quartile ranges for f_e versus $\langle A_b\rangle/\sigma_h^{\mathrm{ref}}$ are 10% larger than when using variable $\langle\sigma_h\rangle$. The improved r_*^2, the binned-mean f_e more power-law consistent, and the smaller quartile range using $\langle A_b\rangle/\langle\sigma_h\rangle$ versus $\langle A_b\rangle/\sigma_h^{\mathrm{ref}}$ (Fig. 7), demonstrate that variable $\langle\sigma_h\rangle$ across instrument pairs is important to setting the wave friction factor and the bottom-friction-induced wave dissipation.

The result above of larger r_*^2 when using $\langle A_b\rangle/\langle\sigma_h\rangle$ instead of $\langle A_b\rangle/\sigma_h^{\mathrm{ref}}$ (Fig. 7) is based on 10 instrument pairs with largest r^2 (from $N = 1$ to $N = 10$, Table 1), where f_e estimates are more reliable. We now assess the sensitivity of this result to the number N of instrument pairs used to compute r_*^2. For $N = 2$ to $N = 15$, r_*^2 was computed using both $\langle\sigma_h\rangle$ and σ_h^{ref} with data from the first N instrument pairs that have highest r^2 (Figure 8b). For $N \leq 10$, using variable $\langle\sigma_h\rangle$ yields $0.28 \leq r_*^2 \leq 0.43$, which is systematically larger than the $0.18 \leq r_*^2 \leq 0.28$ using σ_h^{ref}. For $N > 10$, the r_*^2 decreases for both $\langle\sigma_h\rangle$ and σ_h^{ref}. This is likely due to incorporating higher noise f_e from instrument pairs that have reduced r^2 (Fig. 8a). Nevertheless, even for $N = 14$ where the difference

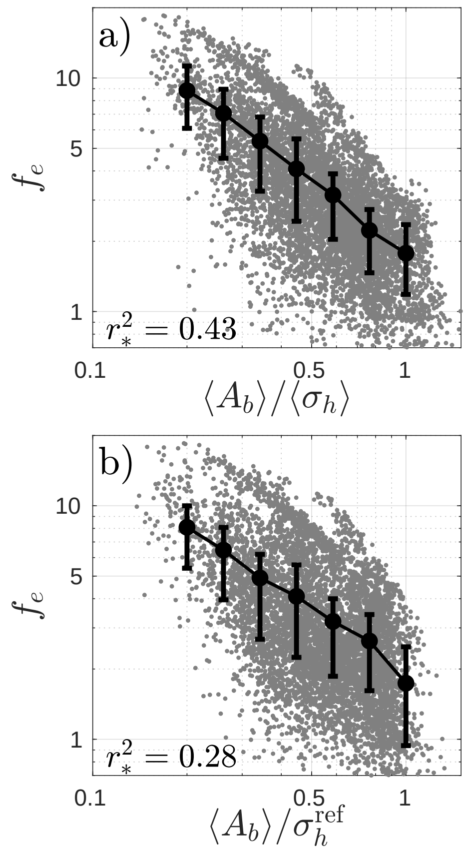

FIG. 7. Friction factor f_e versus (a) $\langle A_b \rangle / \langle \sigma_h \rangle$ and (b) $\langle A_b \rangle / \sigma_h^{\mathrm{ref}}$, where $\langle A_b \rangle$ is the instrument-pair average orbital displacement. Two choices of standard deviation of bed elevation are used: (a) the spatial average between instrument locations for each pair $\langle \sigma_h \rangle$; or (b) a constant average over all pairs $\sigma_h^{\mathrm{ref}} = 0.8$ m. The gray dots are hourly estimates, the black dotted lines are binned means, and the vertical bars denote the 25-75% quartile ranges. Only data from the 10 instrument pairs with the highest correlations ($N \leq 10$) are included. The correlation coefficient squared (a) between $\log_{10}(f_e)$ and $\log_{10}(\langle A_b \rangle / \langle \sigma_h \rangle)$ is $r_*^2 = 0.43$ and (b) between $\log_{10}(f_e)$ and $\log_{10}(\langle A_b \rangle / \sigma_h^{\mathrm{ref}})$ is $r_*^2 = 0.28$.

between results is smallest, the two r_*^2 using $\langle \sigma_h \rangle$ ($r_*^2 = 0.28 \pm 0.02$) and σ_h^{ref} ($r_*^2 = 0.21 \pm 0.02$) are distinct based on the 95% confidence limits. The consistently elevated r_*^2 using $\langle \sigma_h \rangle$ over σ_h^{ref} is a robust result and demonstrates that the spatially variable $\langle \sigma_h \rangle$ partly explains the f_e variability. Therefore, regions with larger $\langle \sigma_h \rangle$ have elevated seabed roughness that induce an increase in f_e.

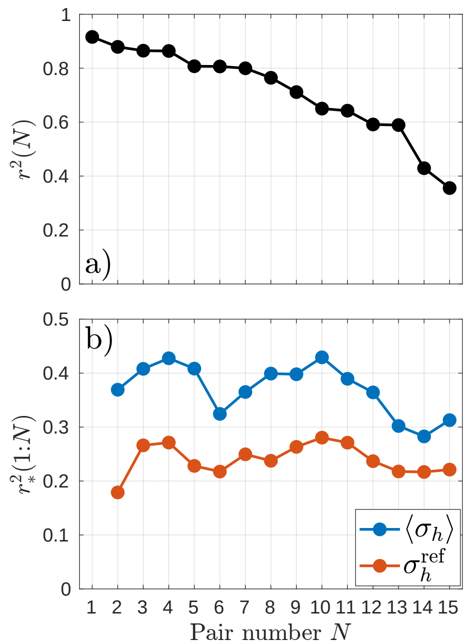

FIG. 8. (a) Correlation coefficient squared r^2 between $\langle U_{\mathrm{rms}} \rangle^3$ and $-\mathrm{d}F/\mathrm{d}x$ versus instrument pair number N passing primary quality control criteria. Results are sorted by largest to smallest r^2, as provided in Table 1. (b) r_*^2 between $\log_{10}(f_e)$ and $\log_{10}\langle A_b \rangle / \langle \sigma_h \rangle$ (blue), and between $\log_{10}(f_e)$ and $\log_{10}(\langle A_b \rangle / \sigma_h^{\mathrm{ref}})$ (orange) for all pairs up to pair number N.

4. Discussion

a. Effect of wave angle on f_e

We assumed normally-incident waves in estimating the cross-shore wave energy flux (10a) and its gradient $\mathrm{d}F/\mathrm{d}x$ (Section 2d). Other f_e studies also require assumptions regarding wave directionality to estimate energy flux from pressure sensors. Generally, wave refraction tends to reduce the incident wave angle in the onshore direction. For studies over reef flats (Lowe et al. 2005; Sous et al. 2023), forereef measurements indicate a small incident mean wave angle, suggesting that assuming unidirectional wave propagation is reasonable. From numerical simulations, refraction across the reef flat was estimated to induce biases in observed $-\mathrm{d}F/\mathrm{d}x$ by 10% at most (Lowe et al. 2005). For f_e estimated on a reef flat, a simple model accounted for refraction, estimating that up to 20–30% of the observed $-\mathrm{d}F/\mathrm{d}x$ could be due to refraction (Falter et al. 2004). For observations in deeper water (5–20 m), Snell's law was applied to offshore directional measurements, assuming alongshore uniform bathymetry, to estimate wave angles at shallower sites with the result that wave directional affects on f_e were small (Monismith et al. 2015; Rogers et al. 2016; Gon et al. 2020). On a reef flat in < 1.5 m water depth, unidirectional waves were assumed (Lentz et al. 2016). On a fore

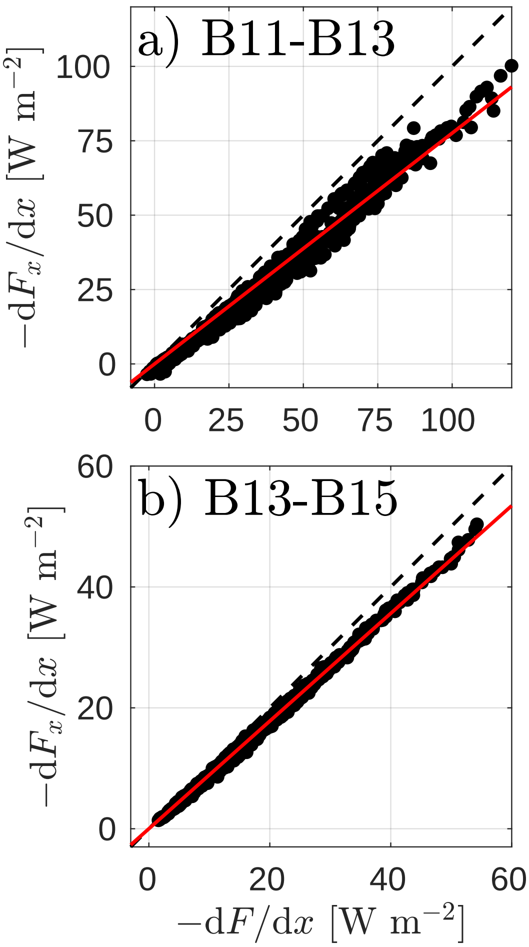

FIG. 9. Scatter plots of the gradients in total flux F (abscissa) and cross-shore flux F_x (ordinate) at two instrument pairs. Cross-shore gradient of the total wave energy flux $-\mathrm{d}F/\mathrm{d}x$ assuming normally incident waves (10a) versus the cross-shore gradient in the cross-shore wave energy flux $-\mathrm{d}F_x/\mathrm{d}x$ accounting for directional information (8a) for instrument pairs (a) B11-B13 and (b) B13-B15. The red solid line is the best-fit linear relationship, and the black dashed line is the 1-to-1 line.

reef with spur-and-groove formations, wave dissipation estimates between ADCPs incorporated the direct measurements of mean wave direction (Acevedo-Ramirez et al. 2021).

However, waves generally have variable incidence angles and are directionally spread. In our study, the mean angles at B03 in 21 m water depth vary from $-30°$ to $40°$ (Fig. 3c), and are directionally spread. Thus, the cross-shore energy flux F_x (8a) is smaller than F (10a), and f_e estimated from $\mathrm{d}F/\mathrm{d}x$ will have a positive bias. However, mean wave angles at B03 are generally $|\theta_{\mathrm{mean}}| < 20°$ (Fig. 3c), and as (neglecting wave directional spread) $\bar{a}_1 \approx \cos(\theta_{\mathrm{mean}})$ and $\cos(20°) = 0.94$, the bias introduced by neglecting directional wave effects is relatively small.

We examine this bias by estimating the cross-shore energy flux F_x at locations where ADCPs were deployed. We do not estimate F_x at Spotter wave buoys as the directional information, particularly in the swell band, is noisy (Collins et al. 2024a). First, directional moments $a_1(f)$ and $b_1(f)$ were computed with (A2)-(A3) based on velocities measured at bins 0.5–1.6 m above the ADCP transducer. Bulk cross-shore (F_x) and alongshore (F_y) wave energy fluxes were computed from (8a)-(8b). From our measurements of $\mathrm{d}F/\mathrm{d}x$ between adjacent sensors, no pairs of ADCPs yielded large r^2 that indicates a reliable f_e estimate. By considering pairs of non-adjacent instruments, data from two ADCP pairs (B11-B13 and B13-B15, Fig. 5a) can be used to compute f_e from the gradient in F_x. The two pairs satisfy the cross-shore spacing criterion, with $\Delta x = 60$ m and $\Delta x = 92$ m, as well as the other primary quality control criteria (Section 3d). At these pairs, the gradients of the total flux $-\mathrm{d}F/\mathrm{d}x$ and of the cross-shore flux $-\mathrm{d}F_x/\mathrm{d}x$ are highly correlated, where the correlation coefficient squared is greater than 0.98 (Fig. 9). Generally, $-\mathrm{d}F_x/\mathrm{d}x$ is smaller than $-\mathrm{d}F/\mathrm{d}x$ with a best-fit slope of 0.78 and 0.89 at B11-B13 and B13-B15, respectively, implying that using $\mathrm{d}F/\mathrm{d}x$ overestimates the wave dissipation by 12%–28%. Larger $-\mathrm{d}F/\mathrm{d}x$ and $-\mathrm{d}F_x/\mathrm{d}x$ are observed at the deeper B11-B13 than in the shallower B13-B15 as wave dissipation decreases the wave energy flux onshore. At these two locations, we also calculate the bulk friction factor $\tilde{f}_e$ using both $\mathrm{d}F/\mathrm{d}x$ and $\mathrm{d}F_x/\mathrm{d}x$. At both pairs, the correlation squared between $\langle U_{\mathrm{rms}}\rangle^3$ and either $\mathrm{d}F/\mathrm{d}x$ or $\mathrm{d}F_x/\mathrm{d}x$ was $r^2 \approx 0.9$, indicating low noise in estimating f_e. At the B11-B13 pair, the bulk friction factor using $-\mathrm{d}F/\mathrm{d}x$ is $\tilde{f}_e = 3.0$, whereas using $-\mathrm{d}F_x/\mathrm{d}x$ results in a reduced $\tilde{f}_e = 2.3$. Similarly, at B13-B15, $\tilde{f}_e = 1.2$ using $-\mathrm{d}F/\mathrm{d}x$ and $\tilde{f}_e = 1.1$ using $-\mathrm{d}F_x/\mathrm{d}x$. These changes in $\tilde{f}_e$ are consistent with the changes between $-\mathrm{d}F/\mathrm{d}x$ and $-\mathrm{d}F_x/\mathrm{d}x$ (Fig. 9b). Overall, this suggests that using $\mathrm{d}F/\mathrm{d}x$ results in a 10%–30% positive bias in friction factor estimates. Even when accounting for this potential bias, the observed bulk $\tilde{f}_e$ (Table 1) are still primarily larger than 1.

b. Challenges of intercomparing results with previous studies

Observational and methodological differences in wave friction factor studies can impact the intercomparison of f_e results. For example, different studies have computed the standard deviation of bottom depth σ_h in different ways due to the available bathymetry data. Hereafter we drop the $\langle\cdot\rangle$ notation. On a coral reef, Lowe et al. (2005) reports σ_h computed within horizontal scales of 0.4–2 m (Nunes and Pawlak 2008). Given the approximately spatially homogeneous bed roughness in their study site, Lowe et al. (2005) averaged σ_h across their entire instrument array and used a single $\sigma_h = 0.035$ m at the locations where f_e was estimated. Monismith et al. (2015) and Rogers et al. (2016) did not provide information about σ_h for their measurements over coral reefs. Lentz et al. (2016) computed a standard deviation of $\sigma_h = 0.13$ m across a single bathymetry transect on a reef flat between one pair of instruments where f_e was estimated. On a coral reef, Sous et al. (2023) computed σ_h between 0.08–0.15 m within horizontal scales 0.1–5 m from bathymetry transects (Sous et al. 2020), and used different σ_h for each of three instrument pairs where wave dissipation was measured. On a rocky seabed, Gon et al. (2020) computed f_e for one instrument pair and estimated $\sigma_h = 0.9$ m from deviations of bed elevation relative to an alongshore averaged bathymetry. Here, on a rocky seabed, σ_h was estimated over horizontal scales less than 20 m and typically larger than 1–4 m (Section 2b), which are longer length scales than other σ_h estimates by Lowe et al. (2005) and (Sous et al. 2023). Across 15 instrument pairs, we computed $0.53 \leq \sigma_h \leq 1.11$ m (Table 1), which is comparable to Gon et al. (2020), and much larger than estimates over coral reefs. Apart from Sous et al. (2023), other studies did not use variable σ_h between multiple instrument pairs. Overall, the difficulty of bathymetry mapping over rough seabeds leads to differences in how σ_h is computed. Therefore, although rocky shores tend to have significantly larger σ_h, differences in the dependency of f_e on σ_h across studies may be partly due to how σ_h is calculated.

Another intercomparison challenge is the different f_e estimation methods. Friction factors have been computed from frequency-dependent or frequency-integrated energy flux gradients, and reported results include timeseries of f_e, time-averaged f_e, as well as $\tilde{f}_e$. From a frequency-dependent energy flux gradient, Lowe et al. (2005) estimated a frequency-dependent f_e and an hourly energy-weighted f_e, and then time-averaged over the experiment duration. Monismith et al. (2015) and Acevedo-Ramirez et al. (2021) estimated $\tilde{f}_e$ from the frequency-integrated energy flux over fore reefs, and noted the high correlation ($r^2 = 0.83$ and $r^2 = 0.9$, respectively) between $-\mathrm{d}F/\mathrm{d}x$ and $\langle U_{\mathrm{rms}} \rangle^3$. Rogers et al. (2016) followed a similar approach to Monismith et al. (2015), but estimated time-dependent f_e at three regions around an atoll. Lentz et al. (2016) also estimated timeseries of f_e from sea-swell-integrated dissipation. Gon et al. (2020) computed hourly friction factors and, although their results show f_e decreasing with A_b, large f_e noise around their bin-means is evident. Sous et al. (2023) used a spectral wave action balance, including nonlinear energy transfers and wave-current interactions, to compute a frequency-dependent friction factor at each hour across a reef flat, and their frequency-integrated f_e have small deviations from binned means as a function of A_b. In our study, frequency-integrated energy flux gradients across 33 instrument pairs were used to compute f_e. Quality control criteria yielded 15 instrument pairs (Table 1) where f_e was estimated, and results were sorted to retain 10 pairs with the highest signal-to-noise ratio inferred from r^2 (Fig. 7). Furthermore, wave dissipation D_f has variable definitions yielding inconsistent f_e and requiring rescaling for a consistent intercomparison (see Appendix B).

c. Intercomparison with previous studies and parameterizing f_e

We now intercompare our results from the ROXSI 2022 experiment with previous field observations on rocky seabeds and coral reefs (Fig. 10). Friction factors from different studies were scaled to account for different definitions of f_e (see Appendix B). For consistency with the dissipation (12), f_e from Lowe et al. (2005) and Sous et al. (2023) were multiplied by 0.875 and the f_e of Lentz et al. (2016) and Gon et al. (2020) were multiplied by 0.5 (Appendix B). Results from Lowe et al. (2005) were taken between 3 instrument pairs, and represent a time-average (over the experiment duration) of the representative friction factor in their spectral model. Both Lentz et al. (2016) and Gon et al. (2020) computed f_e between 1 instrument pair in their experiments, and results were individually bin-averaged in A_b/σ_h. Observations by Sous et al. (2023) yield f_e between 3 instrument pairs, and the time series of the representative friction factor in their spectral model were bin-averaged at each pair independently. We did not intercompare with results from additional field experiments (Monismith et al. 2015; Rogers et al. 2016; Acevedo-Ramirez et al. 2021), because σ_h was not provided.

Results from ROXSI 2022 cover a wide range of water depths from several instrument pairs, typically within $10 \leq \overline{h} \leq 3$ m, with large σ_h (0.7–1.1 m) and A_b (0.15–0.7 m) (Table 1). Our binned-mean f_e are primarily between 2 and 10 for $0.2 \leq A_b/\sigma_h \leq 1$ (black dots in Fig. 10). From an experiment at a different site on the Monterey Peninsula, Gon et al. (2020) estimated binned-mean $1 < f_e < 20$ (red dots, Fig. 10), that are smaller than our results for the same A_b/σ_h with a steeper power-law slope. These results are based on two measurements around $8 \leq \overline{h} \leq 6$ m, with similar σ_h and A_b than in ROXSI 2022. When considering multiple experiments on coral reefs (Lowe et al. 2005; Lentz et al. 2016; Sous et al. 2023), observations of wave dissipation cover a wider range of A_b/σ_h, i.e., from 0.2 to 10, than measurements over rocky seabeds that have $A_b/\sigma_h \leq 1$. For small $A_b/\sigma_h \leq 1$, binned-mean friction factor estimates on coral reefs range from 0.7 to 5, and f_e decreases to 0.2 at large $A_b/\sigma_h \approx 10$. For $A_b/\sigma_h \leq 1$, our binned-mean f_e over a rocky seabed are similar to observations on coral reefs by Sous et al. (2023). The binned-mean f_e from Lentz et al. (2016) are a factor 3-4 smaller than our results for similar A_b/σ_h. We also note that similar A_b/σ_h have distinct A_b and σ_h between rocky seabeds and coral reefs. Small A_b/σ_h on coral reefs typically have both σ_h and A_b smaller than on rocky seabeds by a factor of 2–5, based on observations from shallow reef flats (i.e., $\overline{h} < 2$ m, Lentz et al. 2016; Sous et al. 2023) or forereefs, located in deeper water depths (i.e., $5 \leq \overline{h} < 20$ m, Monismith et al. 2015; Rogers et al. 2016).

Parameterizations of f_e are usually expressed in terms of the roughness parameter k_N (Appendix C). For applying parameterizations to $A_b/k_N \lesssim 1$, it has been suggested (Lowe et al. 2005; Sous et al. 2023; Dealbera et al. 2024) that $k_N \approx 4\sigma_h$. Using $\sigma_h = k_N/4$, we evaluate existing f_e

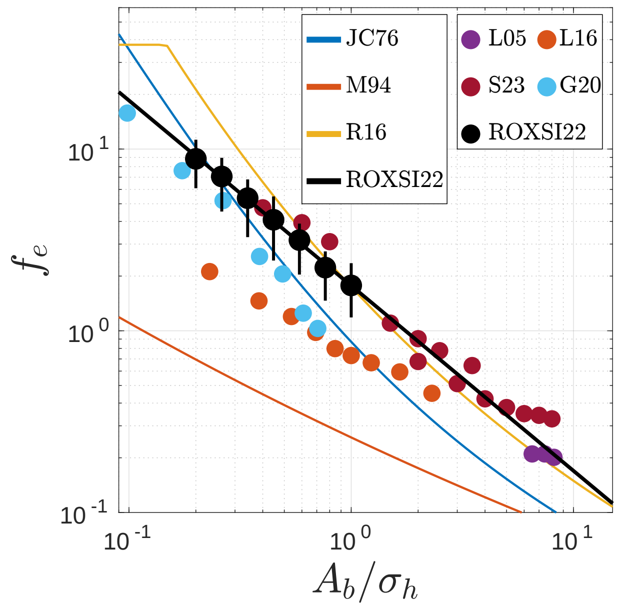

FIG. 10. Bin-averaged f_e vs. A_b/σ_h from the ROXSI 2022 observations (black dots) and the power-law (black line) relationship (15). Observations from previous field experiments are taken from L05 (Lowe et al. 2005), L16 (Lentz et al. 2016), G20 (Gon et al. 2020), and S23 (Sous et al. 2023), where correction factors have been multiplied to results to make definitions of f_e consistent (Appendix B). Curves indicate parameterizations of f_e taken from the literature (Appendix C), and normalized by correction factors in Appendix B: JC76 (Jonsson and Carlsen 1976); M94 (Madsen 1994); and R16 (Rogers et al. 2016). These parameterizations are based on A_b/k_N, and it was assumed that $k_N = 4\sigma_h$ to plot f_e vs. A_b/σ_h.

parameterizations in terms of A_b/σ_h (Fig. 10). We note these parameterizations were developed for $A_b/k_N \gg 1$, or equivalently for $A_b/\sigma_h \gg 4$; thus, technically, the assumptions built into the f_e parameterizations are violated. Parameterizations from Jonsson and Carlsen (1976) and Rogers et al. (2016) roughly predict the magnitude of binned-mean f_e from most experiments, but the relationship between f_e and A_b/σ_h tends to have a steeper slope than in the observations. Several experiments have significantly larger f_e than the maximum friction factor of 0.3 in the parameterization by Madsen et al. (1988) (not shown), which is a standard formulation implemented in numerical wave models (Booij et al. 1999). Although the coefficients in the parameterization from Madsen (1994) have been modified to yield a best-fit to f_e observations (Lowe et al. 2005; Sous et al. 2023; Dealbera et al. 2024), the expression taken directly from Madsen (1994) yields much smaller friction factors than the observations.

Our observations indicate that a power-law parameterization for f_e in terms of A_b/σ_h can be used to model wave transformation over rough seabeds with $0.2 \leq A_b/\sigma_h \leq 1$. Based on the 10 instrument pairs with $r^2 \geq 0.65$ from the ROXSI 2022 experiment (Section 3e), a standard least-squared fit to the bin means of $\log_{10}(f_e)$ and $\log_{10}(A_b/\sigma_h)$ (Fig. 7a) yields

$$f_e = 1.77 \left(\frac{A_b}{\sigma_h}\right)^{-1.02}. \tag{15}$$

The power law (15) from our results over a rocky seabed yield similar f_e than observations from Sous et al. (2023) and Lowe et al. (2005) over coral reefs. The agreement between these results and (15) is within a factor of 2, even for A_b/σ_h up to 10, which is well beyond the regime of our observations. The power law overestimates friction factors from Lentz et al. (2016) by a factor of 3-4, as well as from Gon et al. (2020) for $A_b/\sigma_h > 0.5$, which could be associated with different methodologies (Section 4b) or the importance of incorporating seabed statistics in addition to σ_h (Dealbera et al. 2024). Based on parameterizations for $A_b/\sigma_h \gg 1$ (e.g., Jonsson and Carlsen 1976), the power law (15) will underestimate the friction factor for the smaller roughness of sandy seabeds, such that our parameterization is not valid for very large A_b/σ_h. Nevertheless, the power law (15) provides a simple and practical estimate of f_e within $0.2 \leq A_b/\sigma_h \leq 10$, which is in good agreement with some previous field experiments, and can be used to calculate wave dissipation over environments with rough seabed.

Similar to coral reef measurements, (15) supports that the gradient of f_e with A_b/σ_h is smaller than predicted from expressions like from Jonsson and Carlsen (1976) or Rogers et al. (2016). A power of -1 is in agreement with laboratory studies using roughness elements with length scales between 0.5–1.3 cm (Mirfenderesk and Young 2003) and those using stones and ping-pong balls with sizes of approximately 1.5–4 cm (Dixen et al. 2008). Therefore, extrapolating f_e parameterizations developed for sand grains with $A_b/\sigma_h \gg 1$ may lead to errors in wave dissipation over rough bathymetry, and (15) is more suitable for wave modeling over coral reefs and rocky seabeds.

5. Summary and Conclusions

We presented observations from a month-long experiment, the first field campaign of the ROcky shores: eXperiments and SImulations (ROXSI). Specifically, we examined the cross-shore wave transformation from 20 m water depth to the shoreline at two sites on the rocky shore of the Monterey Peninsula, California, USA. The directly measured seabed was rough with a large standard deviation of bed elevation σ_h of 0.5–1.5 m. The incident significant wave height varied from 0.3–2 m. Significant wave height and cross-shore sea-swell wave energy flux decay onshore of 8-m water depth. These depths are well offshore of the surfzone suggesting that the sea-swell wave energy is attenuated due to bottom friction. Incident mean wave angles in 20-m water depth were largely within ±20° and refracted towards normal incidence in shallower water.

Friction factors f_e were estimated between instrument pairs balancing the cross-shore sea-swell energy flux gradient with the parameterized wave dissipation $D_f = 0.8\rho f_e U_{\mathrm{rms}}^3$, where we computed U_{rms} from pressure measurements and linear-wave theory, and we assumed normally incident waves. Quality control criteria were applied to neglect instrument pairs where f_e estimates were not reliable. Fifteen instrument pairs pass primary quality control criteria with large bulk friction factors varying between 1.0–5, amongst the largest friction factors reported on coral reefs and rocky shores. Additionally, the squared correlation r^2 between the observed flux convergence $-\mathrm{d}F/\mathrm{d}x$ and the cubed bottom orbital velocity $\langle U_{\mathrm{rms}} \rangle^3$ is used as an additional quality control constraint. Ten instrument pairs have $r^2 \geq 0.65$, and their resulting hourly f_e varies between 1–10. For these ten instrument pairs, the hourly f_e consistently increase with smaller A_b/σ_h, the ratio of the orbital amplitude A_b to the standard deviation of seabed elevation σ_h. In log space, f_e and A_b/σ_h are correlated with a maximum $r_*^2 = 0.43$, and binned means of f_e indicate a power-law scaling with A_b/σ_h. We also related f_e to a constant $\sigma_h^{\mathrm{ref}} = 0.8$ m (i.e., the mean σ_h across instrument sites), which reduces r_*^2 to 0.28. Although r_*^2 depends on the number of instrument pairs used when computing r_*^2, the reduction when using σ_h^{ref} instead of σ_h is a robust result. This decrease in r_*^2 demonstrates that our estimate of σ_h is a good proxy for the roughness of the seabed, with larger σ_h enhancing f_e.

Our results are broadly consistent with previous observations of large f_e on coral reefs and rocky shores, and potential sources of discrepancies between studies are discussed. Binned-means of f_e range from 2 to 10 in the ROXSI observations, while previous studies have f_e between 0.7 and 8 for $0.2 \leq A_b/\sigma_h \leq 1$. Although our estimates are based on the assumption of normally-incident waves, directly measured mean wave angles and directional fluxes at a few locations yield a relatively small (10-30%) reduction in f_e. While statistics of seabed variability other than σ_h might be needed to inter-compare results, different methodologies across studies for computing f_e and σ_h might also contribute to discrepancies. Nevertheless, f_e across studies are broadly consistent with a scaling with A_b/σ_h that has a lower slope than predicted by parameterizations developed for small-scale ($A_b/k_N \gg 1$) roughness. The ROXSI observations, based on measurements from a large number of 10 instrument pairs and spanning a wide range of water depths between 3 and 10 m, yield an empirical power-law for f_e in terms of A_b/σ_h, where the power-law exponent is approximately -1. Given this empirical parameterization for f_e, along with high-resolution bathymetry, wave dissipation can be parameterized over the highly rough ($A_b/\sigma_h \leq 1$) seabeds of coral reefs and rocky shores.

Acknowledgments. This paper is part of the ROcky Shore: eXperiment and SImulations (ROXSI) project, funded by the Office of Naval Research through grants N000142112786 and N0001423WX01357. The Monterey NOAA Sanctuary, CA Fish and Wildlife, Pebble Beach, and Pacific Grove provided environmental permission for the experiment and we thank Chris Miller at NPS for support with the permitting process. We thank scientists, students, and technical personnel from SIO, NPS, UNCW, OSU, and UNC-Chapel Hill for their invaluable support with the field experiment; for SIO: Brian Woodward, Kent Smith, Rob Grenzeback, Lucian Parry, Shane Finnerty, Carson Black, Duncan Wheeler, Annie Adelson, Loren Clark, Kaden Quinn, and Kanoa Pick; for NPS: Paul Jessen, Charlotte Benbow, Pat Collins, Mike Cook, Matt Gough, and Ian Jenstrom; for UNCW: Tim Hesford; for OSU: Greg Wilson, Matt Conlin, and June Marion; and for UNC-Chapel Hill: Johanna Rosman, Mika Malila, and Anthony Whipple.

We are grateful to Steve Lentz, Justin Rogers, and Damien Sous for sharing their data with us. We thank Stephen Monismith for sharing his notes, which we strongly borrowed from in Appendix B, and for pointing out that correction factors are necessary to inter-compare friction factors between different studies. OBM appreciates discussions with Matt Conlin and Kaden Quinn. We thank the questions and comments from two reviewers, which helped to improve the manuscript.

Data availability statement. The data presented in this paper will be made freely available upon publication. The code for reproducing the data processing and figures is available at the GitHub repository `github.com/olavobm/Paper_WaveDissipation`.

APPENDIX A

Sea-swell mean period and mean direction

From the sea-surface elevation spectrum S_η, the sea-swell mean wave period is computed as

$$T_{\mathrm{mean}} = \frac{\int_{\mathrm{SS}} S_\eta \, \mathrm{d}f}{\int_{\mathrm{SS}} f S_\eta \, \mathrm{d}f}. \tag{A1}$$

Either sea-surface displacements from wave buoys or pressure and horizontal velocity measurements from ADCPs can be used to calculate standard directional surface wave moments and statistics (e.g., Longuet-Higgins et al. 1963; Kuik et al. 1988; Thomson et al. 2018). For example, directional wave moments can be computed from the x, y, and z components of sea-surface displacement, in terms of their spectra ($S_x(f)$, $S_y(f)$, and $S_z(f)$, respectively) and their cross-spectra.

The first directional moments are computed as

$$a_1(f) = \frac{-Q_{xz}}{\sqrt{S_z(S_x+S_y)}}, \tag{A2}$$

$$b_1(f) = \frac{-Q_{yz}}{\sqrt{S_z(S_x+S_y)}}, \tag{A3}$$

where $Q_{xz}(f)$ and $Q_{yz}(f)$ are the quadrature spectra (i.e., minus the imaginary part of the cross-spectra), between x and z, and between y and z, respectively.

The sea-swell directional moments are computed from energy-weighted averages in frequency space of (A2)-(A3). For example,

$$\overline{a}_1 = \frac{\int_{\mathrm{SS}} a_1 S_\eta \, \mathrm{d}f}{\int_{\mathrm{SS}} S_\eta \, \mathrm{d}f}, \tag{A4}$$

where the subscript SS denotes the $0.05-0.2$ Hz frequency range used throughout this paper for the sea-swell band. Mean direction θ_{mean} was computed as

$$\theta_{\mathrm{mean}} = \tan^{-1}\left(\frac{\overline{b}_1}{\overline{a}_1}\right), \tag{A5}$$

which, along with definitions (A2) and (A3), corresponds to the direction where waves propagate toward relative to the cross-shore (+x).

APPENDIX B

Wave dissipation parameterized by f_e

We compared f_e from previous field measurements (Lowe et al. 2005; Lentz et al. 2016; Gon et al. 2020; Sous et al. 2023) with our results from the ROXSI 2022 experiment (Fig. 10). However, different definitions have been used to express the dissipation in terms of f_e for the various experiments. Here, we examine the f_e definition across studies and present scaling factors (Table B1) to make previous results consistent with our results and equation (12). Much of this Appendix borrows from notes from Prof. Stephen Monismith of Stanford University, for whom we are grateful. The wave energy dissipation factor (f_e), which we and others (e.g., Lentz et al. 2016) commonly refer to as wave friction factor, is defined in terms of the wave energy dissipation D_f as

$$D_f = \rho \frac{f_e}{2} \overline{u^2|u|}, \tag{B1}$$

where the overbar is a time average and u is the horizontal velocity assuming unidirectional wave propagation. For field observations, u is taken as the horizontal velocity evaluated at the seabed from potential flow wave theory (e.g., Lentz et al. 2016). For a monochromatic velocity $u = U_0 \cos(\omega t)$, (B1) yields

$$D_f = \rho \frac{f_e}{2} U_0^3 \overline{\cos^2(\omega t) |\cos(\omega t)|} = \frac{2}{3\pi} \rho f_e U_0^3 \approx 0.21 \rho f_e U_0^3, \tag{B2}$$

and with $U_{\rm rms} = (\overline{u^2})^{1/2} = U_0/\sqrt{2}$, wave dissipation (B2) becomes

$$D_f \approx (0.21 \times 2\sqrt{2}) \rho f_e U_0^3 \approx 0.6 \rho f_e U_{\rm rms}^3. \tag{B3}$$

Jonsson and Carlsen (1976) and Rogers et al. (2016) used (B3) to relate f_e to D_f.

Wave dissipation can also be written in terms of wave height H through linear theory. The peak horizontal velocity at the bottom is related to H by (e.g., Dean and Dalrymple 1991)

$$U_0 = \frac{\omega}{\sinh(kh)} \frac{H}{2}, \tag{B4}$$

where ω is the radian frequency, h is the water depth, and k is the wavenumber evaluated from the dispersion relationship (3). Substituting (B4) into (B3) yields

$$D_f = \frac{1}{12\pi} \rho f_e \left(\frac{\omega}{\sinh(kh)} \right)^3 H^3. \tag{B5}$$

Considering a narrow-band random wave field, wave dissipation becomes (Thornton and Guza 1983),

$$D_f = \frac{1}{12\pi} \rho f_e \left(\frac{\omega_{\rm mean}}{\sinh(k_{\rm mean} h)} \right)^3 \int_0^\infty H^3 p(H) \, \mathrm{dH}, \tag{B6}$$

where $\omega_{\rm mean}$ is the mean wave frequency, $k_{\rm mean}$ is the wavenumber correspondent to $\omega_{\rm mean}$, and $p(H)$ is the Rayleigh probability density function

$$p(H) = \frac{2H}{H_{\rm rms}^2} \exp\left[-\left(\frac{H}{H_{\rm rms}} \right)^2 \right]. \tag{B7}$$

Expression (B6) is equivalent to the dissipation $\langle \epsilon_f \rangle$ in Thornton and Guza (1983), who used the coefficient $c_f \equiv f_e/2$. The integral in (B6) is

$$\int_0^\infty H^3 p(H)\ \mathrm{dH} = \frac{3\sqrt{\pi}}{4} H_{\mathrm{rms}}^3, \tag{B8}$$

resulting in

$$D_f = \frac{1}{16\sqrt{\pi}} \rho f_e \left(\frac{\omega_{\mathrm{mean}}}{\sinh(k_{\mathrm{mean}} h)} \right)^3 H_{\mathrm{rms}}^3. \tag{B9}$$

Thornton and Guza (1983) missed a factor of 2 when evaluating (B8), such that (B9) is twice of the their equation (40) for energy dissipation (Thornton and MacMahan 2024). For a narrow-band wave field,

$$U_{\mathrm{rms}} = \frac{\omega_{\mathrm{mean}}}{\sinh(k_{\mathrm{mean}} h)} \frac{H_{\mathrm{rms}}}{2\sqrt{2}}, \tag{B10}$$

and substituting (B10) into (B9) yields

$$D_f = \sqrt{\frac{2}{\pi}} \rho f_e U_{\mathrm{rms}}^3 \approx 0.8 \rho f_e U_{\mathrm{rms}}^3, \tag{B11}$$

which is equivalent to (12) that we applied to parameterize dissipation in this paper. The dissipation from Lentz et al. (2016) can be written as

$$D_f \approx 0.4 \rho f_e U_{\mathrm{rms}}^3, \tag{B12}$$

which differs from (B11) by a factor of 2 because the correction to Thornton and Guza (1983) was not implemented.

Madsen (1994), Lowe et al. (2005), and Sous et al. (2023) parameterized the spectral wave energy dissipation $\mathcal{D}_f$ in terms of the spectrum of wave velocity denoted as $S_u(\omega)$. The dissipation $\mathcal{D}_f$ was parameterized as

$$\mathcal{D}_f(\omega) = \frac{1}{4} \rho f_e(\omega) u_{b,r} u_b^2(\omega), \tag{B13}$$

where $u_b(\omega) = \sqrt{2 S_u(\omega)}$, and $u_{b,r} = \sqrt{\int u_b^2(\omega)\ \mathrm{d}\omega} = \sqrt{2} U_{\mathrm{rms}}$ is the representative wave velocity as defined by Madsen (1994). In terms of S_u and $U_{\mathrm{rms}} = \sqrt{\int S_u\ \mathrm{d}\omega}$, (B13) can be rewritten as

$$\mathcal{D}_f(\omega) = \frac{\sqrt{2}}{2} \rho f_e(\omega) U_{\mathrm{rms}} S_u(\omega). \tag{B14}$$

TABLE B1. Reference with abbreviation, application type (field data or parameterization), equation representing wave dissipation, and constant multiplied by f_e to make f_e estimates consistent with (B11).

Reference	Type	Equation	constant
Lowe et al. (2005), L05	field data	(B14)	0.875
Lentz et al. (2016), L16	field data	(B12)	0.5
Gon et al. (2020), G20	field data	(B15)	0.5
Sous et al. (2023), S23	field data	(B14)	0.875
Jonsson and Carlsen (1976), JC76	parameterization	(B3)	0.75
Madsen (1994), M94	parameterization	(B14)	0.875
Rogers et al. (2016), R16	parameterization	(B3)	0.75

Gon et al. (2020) also parameterized dissipation spectrally, but used

$$\mathcal{D}_f(\omega) = \frac{\sqrt{2}}{2\sqrt{\pi}}\rho f_e U_{\mathrm{rms}} S_u(\omega), \tag{B15}$$

where f_e is not a function of frequency, and the coefficient is the same as in (B12). For a narrow-band wave spectrum, the integral of $\mathcal{D}_f(\omega)$ over the sea-swell band of (B14) or (B15) yields a dissipation D_f that can be compared with (B11). For the f_e intercomparison (Fig. 10), f_e from other studies were multiplied by the appropriate constants (Table B1) to make all results consistent with (B11).

APPENDIX C

Wave friction factor parameterizations

Several parameterizations for the wave friction factor have been derived for large A_b/k_N, and three solutions are shown in Fig. 10. Here, we present the f_e parameterizations shown in Fig. 10. The wave friction factor f_w in boundary layer theory relates the bottom shear stress to the velocity above the boundary layer (e.g., Jonsson 1966). Measurements of the velocity profile within the boundary layer yield the hydraulic roughness z_0, and $k_N \equiv 30z_0$. Jonsson and Carlsen (1976) presented the semi-empirical parameterization for f_w,

$$\frac{1}{4\sqrt{f_w}} + \log_{10}\frac{1}{4\sqrt{f_w}} = 0.20 + \log_{10}\frac{A_b}{k_N}, \tag{C1}$$

that is valid for $A_b/k_N \gg 1$. Parameterization (C1) is semi-empirical because the form of the equation is theoretically derived for a rough turbulent boundary layer under a monochromatic wave, but the first term on the right-hand side is a coefficient that must be computed from laboratory measurements (Jonsson and Carlsen 1976). Based on earlier laboratory experiments, Jonsson (1966) obtained a coefficient of −0.08 instead of 0.20. For practical purposes, Swart (1974) approximated the f_w solution from Jonsson (1966) as

$$f_w = \exp\left(5.213\left(\frac{A_b}{k_N}\right)^{-0.194} - 5.977\right), \tag{C2}$$

which is accurate to within 3% of the full solution for $A_b/k_N > 1$, but diverges for $A_b/k_N < 1$. Rogers et al. (2016) implemented (C2) in a wave model, but with a maximum of $f_w = 50$ for $A_b/k_N < 0.0369$ to avoid unrealistically large f_w. Nielsen (1992) adjusted the coefficients in (C2) to improve agreement with laboratory measurements in the regime of $A_b/k_N \gg 1$. In Fig. 10, the parameterization JC76 was computed from (C1), and R16 from (C2) with the cut-off $f_w = 50$. Both parameterizations were then normalized according to Table B1. The assumption $f_e = f_w$ was used in Fig. 10, which is commonly assumed for rough turbulent boundary layers (Nielsen 1992).

Grant and Madsen (1979) derived a fully theoretical solution for f_w in a model that includes the combined effect of a current and a monochromatic wave. Madsen (1994) extended the Grant and Madsen (1979) model for a wave spectrum and, based on the approach from Swart (1974), the approximate solution for f_w (without a mean flow) was given as

$$f_w(\omega_r) = \exp\left(7.02\left(\frac{u_{b,r}}{k_N\omega_r}\right)^{-0.078} - 8.82\right), \tag{C3}$$

where $u_{b,r}$ is the same representative velocity as in (B13) and ω_r is the representative wave frequency, defined as the mean radian frequency. Madsen (1994) reports that (C3) is a valid approximation to the full solution of his model within $0.2 \leq u_{b,r}/(k_N\omega_r) \leq 100$. Interestingly, Madsen (1994) claims that his solution is valid for large-scale roughness $u_{b,r}/(k_N\omega_r) \leq 1$. In the absence of a mean flow, the wave energy dissipation in the model by Madsen (1994) is given by (B13), where f_w and f_e were related through

$$f_e = f_w\cos(\Theta), \qquad \Theta(\omega_r) = 33 - 6.0\log_{10}\left(\frac{u_{b,r}}{k_N\omega_r}\right), \tag{C4}$$

where Θ is in degrees. Madsen (1994) stated that, for $0.2 \leq u_{b,r}/(k_N\omega_r) \leq 1000$, the approximation (C4) is accurate to within 1% of the full solution.

Both Lowe et al. (2005) and Sous et al. (2023) cited Madsen (1994) to compare their observed f_e with theory, and to compute k_N. Lowe et al. (2005) used an spectral f_e parameterization with the same form as (C3)–(C4), but with the coefficients that Nielsen (1992) modified from Swart (1974). Sous et al. (2023) followed Madsen (1994), including the effect of the mean flow, but all the coefficients in (C3) were changed to provide a best-fit to the observations. Since (C3)–(C4) is based on a fully theoretical model, the coefficients in (C3) should not be changed, and Lowe et al. (2005) and Sous et al. (2023) did not apply Madsen (1994)'s model. Given that the coefficients in the expressions used by Lowe et al. (2005) and Sous et al. (2023) are based on an adjustment of the parameterizations to observations, the model by Madsen (1994) does not agree with measurements for $A_b/k_N < 20$ (Fig. 10). The f_e denoted as M94 in Fig. 10 was computed from (C3)-(C4) after substituting $A_b = u_{b,r}/\omega_r$ and $k_N = 4\sigma_h$, as suggested by Lowe et al. (2005) and Sous et al. (2023). The M94 parameterization was normalized according to Table B1.

References

Acevedo-Ramirez, C. A., W. Stephenson, S. Wakes, and I. Mariño-Tapia, 2021: Wave transformation on a fringing reef system with spur and groove structures. *Journal of Geophysical Research: Oceans*, **126 (9)**, e2020JC016 910, https://doi.org/10.1029/2020JC016910.

Amador, A., I. B. Arzeno, S. N. Giddings, M. A. Merrifield, and G. Pawlak, 2020: Cross-shore structure of tidally driven alongshore flow over rough bathymetry. *Journal of Geophysical Research: Oceans*, **125 (8)**, https://doi.org/10.1029/2020JC016264.

Barnard, P. L., L. H. Erikson, and R. G. Kvitek, 2011: Small-scale sediment transport patterns and bedform morphodynamics: new insights from high-resolution multibeam bathymetry. *Geo-Marine Letters*, **31 (4)**, 227–236, https://doi.org/10.1007/s00367-011-0227-1.

Barr, B. C., D. N. Slinn, T. Pierro, and K. B. Winters, 2004: Numerical simulation of turbulent, oscillatory flow over sand ripples. *Journal of Geophysical Research: Oceans*, **109 (C9)**, https://doi.org/10.1029/2002JC001709.

Bishop, C., and M. Donelan, 1987: Measuring waves with pressure transducers. *Coastal Engineering*, **11 (4)**, 309–328, https://doi.org/10.1016/0378-3839(87)90031-7.

Booij, N., R. Ris, and L. Holthuijsen, 1999: A third-generation wave model for coastal regions - 1. model description and validation. *Journal of Geophysical Research: Oceans*, **104 (C4)**, 7649–7666, https://doi.org/10.1029/98JC02622.

Chung, D., N. Hutchins, M. P. Schultz, and K. A. Flack, 2021: Predicting the drag of rough surfaces. **53**, 439–471, https://doi.org/10.1146/annurev-fluid-062520-115127.

Collins, C. O., and Coauthors, 2024a: Performance of moored gps wave buoys. *Coastal Engineering Journal*, **66 (1, SI)**, 17–43, https://doi.org/10.1080/21664250.2023.2295105.

Collins, P., J. MacMahan, E. Thornton, C. Benbow, and P. Jessen, 2024b: Beach and backward bragg sea-swell wave reflection across rocky and sandy shores. *Journal of Geophysical Research: Oceans*, **129 (11)**, e2023JC020 177, https://doi.org/10.1029/2023JC020177.

CSUMB, Seafloor Mapping Lab, 2014: California Seafloor Mapping Project – Undersea Imagery Archive 2007-2014. Accessed: 2022, https://csumb.edu/undersea/seafloor-maps.

Dalrymple, R. A., J. H. MacMahan, A. J. Reniers, and V. Nelko, 2010: Rip currents. *Annual Review of Fluid Mechanics*, **42**, 551–581, https://doi.org/10.1146/annurev-fluid-122109-160733.

Davis, K. A., G. Pawlak, and S. G. Monismith, 2021: Turbulence and coral reefs. *Annual Review of Marine Science*, **13**, 343–373, https://doi.org/10.1146/annurev-marine-042120-071823.

Dealbera, S., D. Sous, D. Morichon, and H. Michaud, 2024: The role of roughness geometry in frictional wave dissipation. *Coastal Engineering*, **189**, https://doi.org/10.1016/j.coastaleng.2024.104478.

Dean, R. G., and R. A. Dalrymple, 1991: *Water Wave Mechanics for Engineers and Scientists*, Vol. 2. World Scientific Publishing Company.

Denny, M., 1995: Predicting physical disturbance: Mechanistic approaches to the study of survivorship on wave-swept shores. *Ecological Monographs*, **65 (4)**, 371–418, https://doi.org/10.2307/2963496.

Dixen, M., F. Hatipoglu, B. M. Sumer, and J. Fredsoe, 2008: Wave boundary layer over a stone-covered bed. *Coastal Engineering*, **55 (1)**, 1–20, https://doi.org/10.1016/j.coastaleng.2007.06.005.

Emery, W., and R. Thomson, 2014: *Data Analysis Methods in Physical Oceanography*. 1-716 pp.

Falter, J., M. Atkinson, and M. Merrifield, 2004: Mass-transfer limitation of nutrient uptake by a wave-dominated reef flat community. *Limnology and Oceanography*, **49 (5)**, 1820–1831, https://doi.org/10.4319/lo.2004.49.5.1820.

Feddersen, F., R. T. Guza, S. Elgar, and T. H. C. Herbers, 1998: Alongshore momentum balances in the nearshore. *Journal of Geophysical Research: Oceans*, **103 (C8)**, 15 667–15 676, https://doi.org/10.1029/98JC01270.

Flack, K. A., and M. P. Schultz, 2010: Review of Hydraulic Roughness Scales in the Fully Rough Regime. *Journal of Fluids Engineering*, **132 (4)**, 041 203, https://doi.org/10.1115/1.4001492.

Gerritsen, F., 1980: Wave attenuation and wave set-up on a coastal reef. *Coastal Engineering 1980*, 444–461, https://doi.org/10.1061/9780872622647.028.

Gon, C. J., J. H. MacMahan, E. B. Thornton, and M. Denny, 2020: Wave dissipation by bottom friction on the inner shelf of a rocky shore. *Journal of Geophysical Research: Oceans*, **125 (10)**, https://doi.org/10.1029/2019JC015963.

Grant, W., and O. Madsen, 1979: Combined wave and current interaction with a rough bottom. *Journal of Geophysical Research: Oceans*, **84 (NC4)**, 1797–1808, https://doi.org/10.1029/JC084iC04p01797.

Guza, R., and E. B. Thornton, 1980: Local and shoaled comparisons of sea surface elevations, pressures, and velocities. *Journal of Geophysical Research: Oceans*, **85 (C3)**, 1524–1530, https://doi.org/https://doi.org/10.1029/JC085iC03p01524.

Hardy, T. A., and I. R. Young, 1996: Field study of wave attenuation on an offshore coral reef. *Journal of Geophysical Research: Oceans*, **101 (C6)**, 14 311–14 326.

Herbers, T., S. Elgar, and R. Guza, 1994: Infragravity-frequency (0.005-0.05 hz) motions on the shelf. part I: Forced waves. *Journal of Physical Oceanography*, **24 (5)**, 917–927, https://doi.org/10.1175/1520-0485(1994)024⟨0917:IFHMOT⟩2.0.CO;2.

Herbers, T., S. Elgar, and R. Guza, 1999: Directional spreading of waves in the nearshore. *Journal of Geophysical Research: Oceans*, **104 (C4)**, 7683–7693, https://doi.org/10.1029/1998JC900092.

Herbers, T. H. C., P. F. Jessen, T. T. Janssen, D. B. Colbert, and J. H. MacMahan, 2012: Observing ocean surface waves with gps-tracked buoys. *Journal of Atmospheric and Oceanic Technology*, **29 (7)**, 944 – 959, https://doi.org/10.1175/JTECH-D-11-00128.1.

Huang, Z.-C., L. Lenain, W. K. Melville, J. H. Middleton, B. Reineman, N. Statom, and R. M. McCabe, 2012: Dissipation of wave energy and turbulence in a shallow coral reef lagoon. *Journal of Geophysical Research: Oceans*, **117 (C3)**.

Jonsson, I. G., 1966: Wave boundary layers and friction factors. *Coastal engineering*, 127–148.

Jonsson, I. G., and N. A. Carlsen, 1976: Experimental and theoretical investigations in an oscillatory turbulent boundary layer. *Journal of Hydraulic Research*, **14 (1)**, 45–60.

Kamphuis, J., 1974: Determination of sand roughness for fixed beds. *Journal of Hydraulic Research*, **12 (2)**, 193–203.

Kamphuis, J., 1975: Friction factor under oscillatory waves. *Journal of the Waterways, Harbors, and Coastal Engineering Division-ASCE*, **101 (NWW2)**, 135–144.

Kuik, A. J., G. P. Van Vledder, and L. H. Holthuijsen, 1988: A method for the routine analysis of pitch-and-roll buoy wave data. *Journal of Physical Oceanography*, **18 (7)**, 1020–1034, https://doi.org/10.1175/1520-0485(1988)018.

Lentz, S. J., J. H. Churchill, K. A. Davis, and J. T. Farrar, 2016: Surface gravity wave transformation across a platform coral reef in the red sea. *Journal of Geophysical Research: Oceans*, **121 (1)**, 693–705, https://doi.org/10.1002/2015JC011142.

Longuet-Higgins, M., D. Cartwright, and N. Smith, 1963: *Ocean Wave Spectra*, chap. Observations of the Directional Spectrum of Sea Waves Using the Motions of a Floating Buoy, 111–136. Prentice Hall.

Lowe, R., J. Falter, M. Bandet, G. Pawlak, M. Atkinson, S. Monismith, and J. Koseff, 2005: Spectral wave dissipation over a barrier reef. *Journal of Geophysical Research: Oceans*, **110 (C4)**, https://doi.org/10.1029/2004JC002711.

Lowe, R. J., J. L. Falter, J. R. Koseff, S. G. Monismith, and M. J. Atkinson, 2007: Spectral wave flow attenuation within submerged canopies: Implications for wave energy dissipation. *Journal of Geophysical Research: Oceans*, **112 (C5)**, https://doi.org/https://doi.org/10.1029/2006JC003605.

MacMahan, J., E. Thornton, S. Dressel, and M. Cook, 2024: Intermediate wave scale rocky bottom variability for the nearshore along california. *Journal of Geophysical Research: Earth Surface*, submitted, revision.

Madsen, O. S., 1994: Spectral wave-current bottom boundary layer flows. *Coastal Engineering*, 384–398, https://doi.org/10.1061/9780784400890.030.

Madsen, O. S., Y.-K. Poon, and H. C. Graber, 1988: Spectral wave attenuation by bottom friction: Theory. *Coastal Engineering*, 492–504, https://doi.org/10.1061/9780872626874.035.

Marques, O., F. Feddersen, and J. MacMahan, 2024: An effective water depth correction for pressure-based wave statistics on rough bathymetry. *JTECH*, submitted, revision.

Mirfenderesk, H., and I. Young, 2003: Direct measurements of the bottom friction factor beneath surface gravity waves. *Applied Ocean Research*, **25 (5)**, 269–287, https://doi.org/10.1016/j.apor.2004.02.002.

Monismith, S. G., 2007: Hydrodynamics of coral reefs. *Annual Review of Fluid Mechanics*, **39**, 37–55, https://doi.org/10.1146/annurev.fluid.38.050304.092125.

Monismith, S. G., J. S. Rogers, D. Koweek, and R. B. Dunbar, 2015: Frictional wave dissipation on a remarkably rough reef. *Geophysical Research Letters*, **42 (10)**, 4063–4071, https://doi.org/10.1002/2015GL063804.

Moulton, M., S. H. Suanda, J. C. Garwood, N. Kumar, M. R. Fewings, and J. M. Pringle, 2023: Exchange of plankton, pollutants, and particles across the nearshore region. *Annual Review of Marine Science*, **15**, 167–202, https://doi.org/10.1146/annurev-marine-032122-115057.

Nelson, R., 1996: Hydraulic roughness of coral reef platforms. *Applied Ocean Research*, **18 (5)**, 265–274, https://doi.org/10.1016/S0141-1187(97)00006-0.

Nielsen, P., 1992: *Coastal bottom boundary layers and sediment transport*, Vol. 4. World scientific.

Nunes, V., and G. Pawlak, 2008: Observations of bed roughness of a coral reef. *Journal of Coastal Research*, **24 (2B, S)**, 39–50, https://doi.org/10.2112/05-0616.1.

OCM Partners, 2024: 2013 NOAA Coastal California Topobathy Merge Project. Accessed: 2024-05-19, https://www.fisheries.noaa.gov/inport/item/49649.

Péquignet, A.-C., J. M. Becker, M. Merrifield, and S. Boc, 2011: The dissipation of wind wave energy across a fringing reef at ipan, guam. *Coral Reefs*, **30**, 71–82, https://doi.org/10.1007/s00338-011-0719-5.

Poate, T., G. Masselink, M. J. Austin, M. Dickson, and R. McCall, 2018: The role of bed roughness in wave transformation across sloping rock shore platforms. *Journal of Geophysical Research: Earth Surface*, **123 (1)**, 97–123, https://doi.org/10.1002/2017JF004277.

Raghukumar, K., G. Chang, F. Spada, C. Jones, T. Janssen, and A. Gans, 2019: Performance characteristics of “spotter,” a newly developed real-time wave measurement buoy.

Journal of Atmospheric and Oceanic Technology, **36 (6)**, 1127 – 1141, https://doi.org/10.1175/JTECH-D-18-0151.1.

Rogers, J. S., S. A. Maticka, V. Chirayath, C. B. Woodson, J. J. Alonso, and S. G. Monismith, 2018: Connecting flow over complex terrain to hydrodynamic roughness on a coral reef. *Journal of Physical Oceanography*, **48 (7)**, 1567–1587, https://doi.org/10.1175/JPO-D-18-0013.1.

Rogers, J. S., S. G. Monismith, D. A. Koweek, and R. B. Dunbar, 2016: Wave dynamics of a pacific atoll with high frictional effects. *Journal of Geophysical Research: Oceans*, **121 (1)**, 350–367, https://doi.org/10.1002/2015JC011170.

Rosman, J. H., and J. L. Hench, 2011: A framework for understanding drag parameterizations for coral reefs. *Journal of Geophysical Research: Oceans*, **116**, https://doi.org/10.1029/2010JC006892.

Ruessink, B., J. Miles, F. Feddersen, R. Guza, and S. Elgar, 2001: Modeling the alongshore current on barred beaches. *Journal of Geophysical Research: Oceans*, **106 (C10)**, 22 451–22 463, https://doi.org/10.1029/2000JC000766.

Sallenger, A., and R. Holman, 1985: Wave energy saturation on a natural beach of variable slope. *JOURNAL OF GEOPHYSICAL RESEARCH-OCEANS*, **90 (NC6)**, 1939–1944, https://doi.org/10.1029/JC090iC06p11939.

Sherwood, C. R., and Coauthors, 2022: Modeling the morphodynamics of coastal responses to extreme events: What shape are we in? *Annual Review of Marine Science*, **14**, 457–492, https://doi.org/10.1146/annurev-marine-032221-090215.

Simons, R. R., A. J. Grass, and A. Kyriacou, 1988: The influence of currents on wave attenuation. 363–376, https://doi.org/10.1061/9780872626874.026.

Sleath, J., 1987: Turbulent oscillatory flow over rough beds. *Journal of Fluid Mechanics*, **182**, 369–409.

Smyth, C., and A. E. Hay, 2003: Near-bed turbulence and bottom friction during sandyduck97. *Journal of Geophysical Research: Oceans*, **108 (C6)**, https://doi.org/https://doi.org/10.1029/2001JC000952.

Sous, D., F. Bouchette, E. Doerflinger, S. Meule, R. Certain, G. Toulemonde, B. Dubarbier, and B. Salvat, 2020: On the small-scale fractal geometrical structure of a living coral reef barrier. *Earth Surface Processes and Landforms*, **45 (12)**, 3042–3054, https://doi.org/10.1002/esp.4950.

Sous, D., K. Martins, M. Tissier, F. Bouchette, and S. Meule, 2023: Spectral wave dissipation over a roughness-varying barrier reef. *Geophysical Research Letters*, **50 (5)**, https://doi.org/10.1029/2022GL102104.

Swart, D. H., 1974: Offshore sediment transport and equilibrium beach profiles. *Delft Hydraulics, Pub.*, **131**.

Thomson, J., J. B. Girton, R. Jha, and A. Trapani, 2018: Measurements of directional wave spectra and wind stress from a wave glider autonomous surface vehicle. *Journal of Atmospheric and Oceanic Technology*, **35 (2)**, 347–363, https://doi.org/10.1175/JTECH-D-17-0091.1.

Thornton, E., and R. Guza, 1982: Energy saturation and phase speeds measured on a natural beach. *Journal of Geophysical Research: Oceans*, **87 (NC12)**, 9499–9508, https://doi.org/10.1029/JC087iC12p09499.

Thornton, E., and R. Guza, 1983: Transformation of wave height distribution. *Journal of Geophysical Research: Oceans*, **88 (NC10)**, 5925–5938, https://doi.org/10.1029/JC088iC10p05925.

Thornton, E. B., and J. MacMahan, 2024: Update to friction factor formulations that impact rocky shores and coral reefs. *Journal of Geophysical Research: Oceans*, **129 (11)**, e2024JC021 630, https://doi.org/10.1029/2024JC021630.

Yu, X., J. H. Rosman, and J. L. Hench, 2018: Interaction of waves with idealized high-relief bottom roughness. *Journal of Geophysical Research: Oceans*, **123 (4)**, 3038–3059, https://doi.org/10.1029/2017JC013515.